ACS Energy LETTERS

Cite This: ACS Energy Lett. 2019, 4, 1342−1348

http://pubs.acs.org/journal/aelccp

LETTER

A Water-Miscible Quinone Flow Battery with High Volumetric Capacity and Energy Density

Shijian Jin,[†,▽] Yan Jing,[‡,▽] David G. Kwabi,[†,§] Yunlong Ji,[‡] Liuchuan Tong,[‡] Diana De Porcellinis,[†] Marc-Antoni Goulet,[†] Daniel A. Pollack,[#] Roy G. Gordon,[*,†,‡] and Michael J. Aziz[*,†]

[†]John A. Paulson School of Engineering and Applied Sciences, Harvard University, Cambridge, Massachusetts 02138, United States

[‡]Department of Chemistry and Chemical Biology, Harvard University, Cambridge, Massachusetts 02138, United States

[#]Department of Physics, Harvard University, Cambridge, Massachusetts 02138, United States

Supporting Information

ABSTRACT: A water-miscible anthraquinone with polyethylene glycol (PEG)-based solubilizing groups is introduced as the redox-active molecule in a negative electrolyte (negolyte) for aqueous redox flow batteries, exhibiting the highest volumetric capacity among aqueous organic negolytes. We synthesized and screened a series of PEG-substituted anthraquinones (PEGAQs) and carefully studied one of its isomers, namely, 1,8-bis(2-(2-(2-hydroxyethoxy)ethoxy)-ethoxy)anthracene-9,10-dione (AQ-1,8-3E-OH), which has high electrochemical reversibility and is completely miscible in water of any pH. A negolyte containing 1.5 M AQ-1,8-3E-OH, when paired with a ferrocyanide-based positive electrolyte across an inexpensive, nonfluorinated permselective polymer membrane at pH 7, exhibits an open-circuit potential of 1.0 V, a volumetric capacity of 80.4 Ah/L, and an energy density of 25.2 Wh/L.

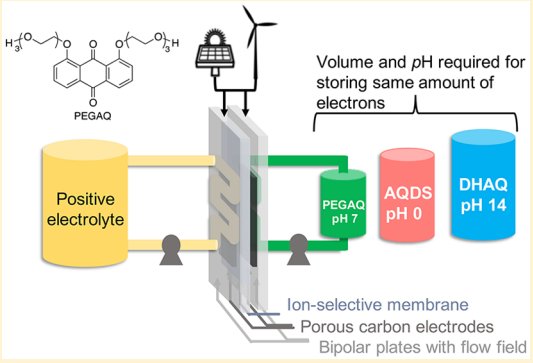

Renewable energy resources such as solar and wind energy are expected to replace fossil fuels for generating electricity.[1] However, the intermittent availability of renewable energy hampers its deep penetration into the electrical grid.[2] Safe, low-cost, grid-scale energy storage could solve this problem.[3] Aqueous redox flow batteries (ARFBs) featuring low-cost and nonflammable electrolytes, as well as decoupled energy/power scaling, are particularly suitable for storing massive amounts of electricity generated from renewables.[4,5] The vanadium redox flow battery has been the most developed ARFB, but the high price and low abundance of vanadium limits its widespread deployment.[6,7] Redox-active organic molecules comprising earth abundant elements such as C, H, O, and N are potentially more cost-effective[8] and scalable. Moreover, the structural diversity and tunability of organics allows chemists to design molecules with important properties, such as high solubility, fast kinetics, appropriate redox potentials, and high stability.

The potential cost of organic redox molecules has been projected to be extremely low.[9,10] Recently, organic molecules with very long projected lifetimes have been developed as negative electrolyte (negolyte) molecules in ARFBs.[11−14] However, these organic molecules tend to have lower solubilities than vanadium species, resulting in considerably lower volumetric capacities for the resulting electrolytes.[15] Although the energy capacity can be scaled up by increasing the volume of electrolyte reservoirs, the size of electrolyte reservoirs may be constrained by available space and cost. Therefore, besides safety, low material cost, and long lifetime, storing as many electrons as possible per unit volume, i.e., having a high volumetric capacity, is another valuable attribute for electrolytes, particularly where ARFBs are deployed in high population-density areas. In such cases, the physical space used for accommodating electrolyte tanks may contribute significantly to the total capital cost of ARFBs.[16] One strategy is to increase the aqueous solubility of redox active materials (RAMs). Ionic groups such as $-SO_3^-$,[13,15,17,18] $-O^-$,[9,19] $-COO^-$,[11,15,20,21] $-PO_3^{2-}$,[14] and $-NR_3^+$[12,20] have been tethered to RAMs such as quinones, viologen, phenazine, ferrocene, and (2,2,6,6-tetramethylpiperidin-1-yl)oxyl (TEMPO) to increase solubility; and molecules bearing these functional groups can demonstrate >1 M electron-storing capability. Frequently the solubility is heavily dependent on the electrolyte pH, and corresponding flow cells must be operated within certain pH ranges to achieve adequate capacity; otherwise, RAMs precipitate because of changes in the protonation state or decomposition of ionic groups.

Received: April 5, 2019
Accepted: May 16, 2019
Published: May 22, 2019

DOI: 10.1021/acsenergylett.9b00739
ACS Energy Lett. 2019, 4, 1342−1348

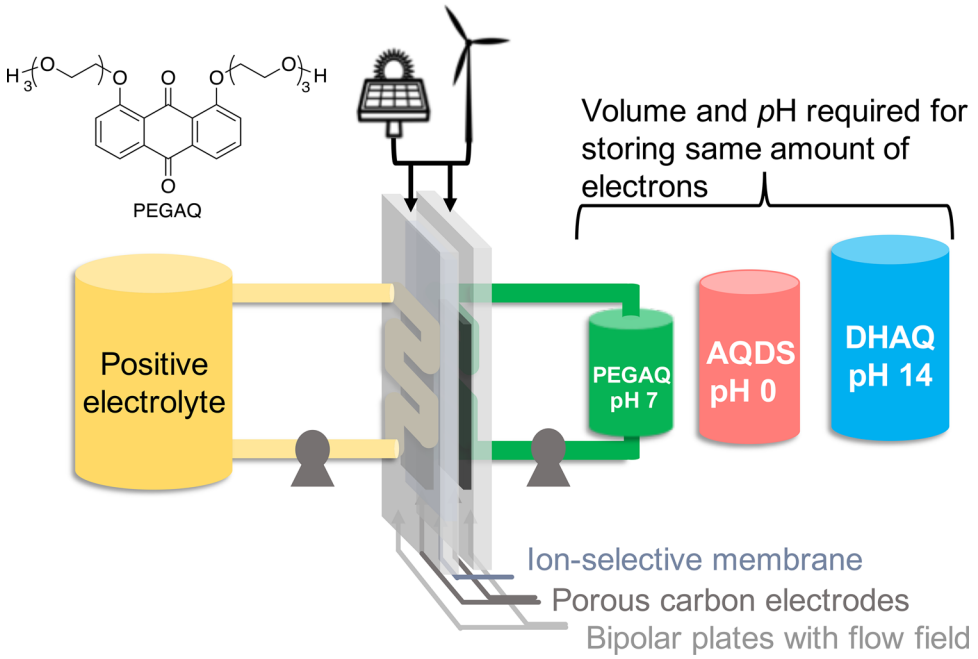

Figure 1. Schematic flow battery with three different negative electrolytes (negolytes): PEGAQ, AQDS,[18] and DHAQ.[22] The pH and volume required to store the same number of electrons are highlighted for each.

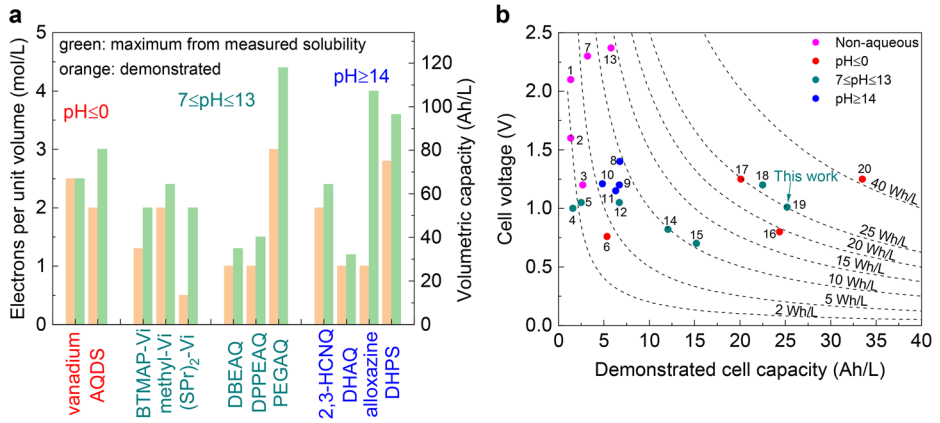

Figure 2. Electrons stored per unit/volumetric capacity of negolytes and comparisons of demonstrated cell capacity/energy densities. (a) From left to right: in strong acid (pH ≤ 0): vanadium,[7] AQDS;[18] neutral (pH ∼7): BTMAP-Vi,[12] Methyl-Vi,[20] $(SPr)_2$-Vi;[17] near neutral (7 ≤ pH ≤ 13): DBEAQ,[11] DPPEAQ,[14] PEGAQ (AQ-1,8-3E-OH); in strong base (pH ≥ 14): 2,3-HCNQ,[21] DHAQ,[19] alloxazine,[23] and DHPS.[15] The orange bars represent demonstrated values in flow cells; the green bars represent maximum values calculated from measured solubilities. (b) The redox couples are listed as negolyte/posolyte. 1, $V(acac)_3/V(acac)_3$;[24] 2, FL/DMPZ;[25] 3, methyl-ViTFSI/FcNTFSI;[26] 4, $DPPEAQ/K_4Fe(CN)_6$;[14] 5, $DBEAQ/K_4Fe(CN)_6$;[11] 6, AQS/BQDS;[27] 7, MePh/DBMMB;[28] 8, $DHPS/K_4Fe(CN)_6$;[15] 9, $DHAQ/K_4Fe(CN)_6$;[22] 10, $DHBQ/K_4Fe(CN)_6$;[9] 11, $alloxazine/K_4Fe(CN)_6$;[23] 12, Methyl-Vi/FcNCl;[29] 13, FL/DBMMB;[30] 14, $(SPr)_2$-Vi/$(NH_4)_4Fe(CN)_6$;[13] 15, BTMAP-Vi/BTMAP-Fc;[12] 16, AQDS/HBr;[31] 17, vanadium/vanadium (supporting electrolyte: H_2SO_4);[32] 18, methyl-Vi/TEMPTMA;[20] 19, $PEGAQ/K_4Fe(CN)_6$:$Na_4Fe(CN)_6$ (1:1); 20, vanadium/vanadium (supporting electrolyte: H_2SO_4/HCl mixture).[7]

Scheme 1. Synthetic Conditions of PEGylated Anthraquinone Isomers through One-Step Williamson Etherification

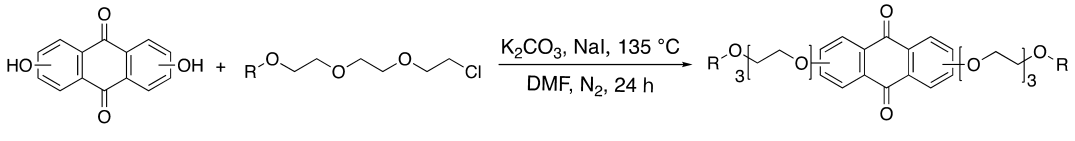

R: –H, –CH_3

AQ–*n,m*–3E–(OR)

R: –H *n, m* = **a**: 1, 2 **b**: 1, 4 **c**: 1, 5 **d**: 1, 8 **e**: 2, 6 **f**: 2, 7

R: –CH_3 *n, m* = **g**: 1, 8

DOI: 10.1021/acsenergylett.9b00739
ACS Energy Lett. 2019, 4, 1342−1348

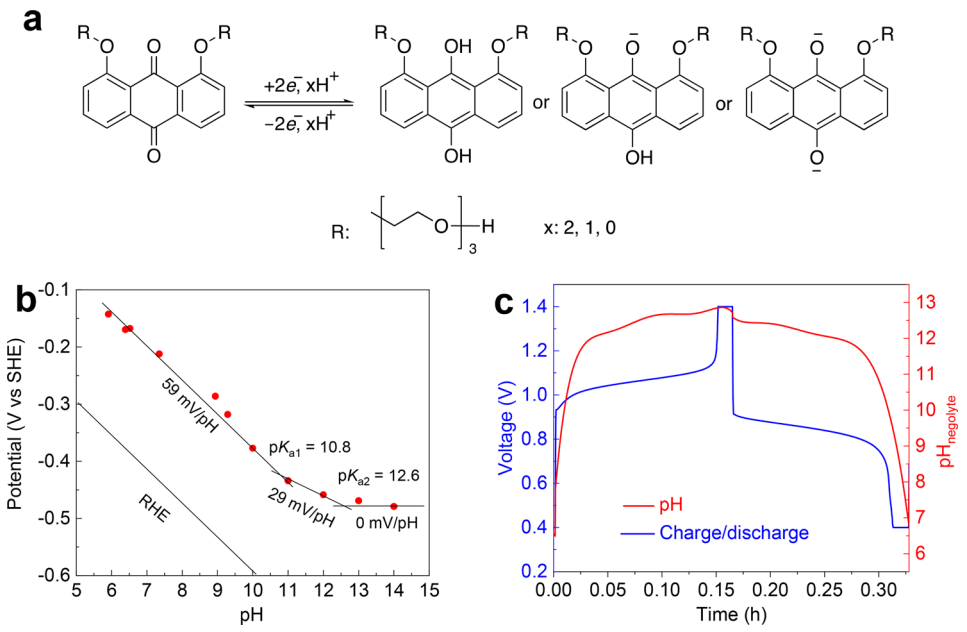

Figure 3. pH-related properties of AQ-1,8-3E-OH. (a) Scheme of the three different reduction products of the anthraquinone. (b) Pourbaix diagram of AQ-1,8-3E-OH with a line of constrained slope of −59 mV/pH fit to the data for pH 6−10 and a constrained slope of −29 mV/pH for pH 10−12.5. Above pH ∼12.6, the potential is pH-independent, indicating that the reduced form of AQ-1,8-3E-OH is deprotonated. The lines of slope 59, 29, and 0 mV/pH are simply guides to the eye. All of the potentials were determined by cyclic voltammograms of 10 mM AQ-1,8-3E-OH in buffered solutions. (c) Charging of AQ-1,8-3E-OH increases the pH of the solution, and discharging reverses the pH change. Electrolytes comprised 7 mL of 0.1 M AQ-1,8-3E-OH (negolyte) in 1 M KCl and 40 mL of 0.1 M potassium ferrocyanide and 0.04 M potassium ferricyanide (posolyte) in 1 M KCl. The applied current density was 50 mA/cm^2.

In this work, we incorporate a nonionic but water-miscible motif, i.e., triethylene glycol, into an anthraquinone through the well-developed one-step Williamson ether synthesis and report a water-miscible RAM, 1,8-bis(2-(2-(2-hydroxyethoxy)-ethoxy)ethoxy)anthracene-9,10-dione (**AQ-1,8-3E-OH**), as a negolyte (Figure 1). Its pH-independent water miscibility enables us to prepare 1.5 M **AQ-1,8-3E-OH** at pH 7 and demonstrate a volumetric capacity of 80.4 Ah/L, which is the highest volumetric capacity reported to date among all aqueous organic negolytes (Figure 2). Pairing the negolyte with a 1.5 M ferrocyanide positive electrolyte (posolyte) at pH 7, our flow cell exhibits an open-circuit voltage of 1.0 V and an energy density of 25.2 Wh/L, which is one of the highest energy densities among all organic aqueous or nonaqueous flow batteries and is even comparable with most vanadium flow batteries.

Samples of 1,2-, 1,4-, 1,5-, 1,8-, 2,6-, 2,7-bis(2-(2-(2-hydroxyethoxy)ethoxy)ethoxy)anthracene-9,10-dione (AQ-*n,m*-3E-OH) and 1,8-bis(2-(2-(2-methoxyethoxy)ethoxy)-ethoxy)anthracene-9,10-dione (AQ-1,8-3E-OCH$_3$) were obtained through one-step Williamson etherification[33] (Scheme 1) (^{1}H and ^{13}C NMR spetra in Figures S1 and S2). After measuring their solubilities (Figure S3) and evaluating reaction kinetics via cyclic voltammetry (CV) (see the Supporting Information, Solubility Measurements, pp 11−13, and Electochemical Characterization, pp 13−15, for more details), we set out to further investigate the electrochemical properties of **AQ-1,8-3E-OH** for use as the RAM in a negolyte because of its high solubility and rapid kinetics (Figures S6−S8).

On the basis of the CV results, the reduction potential ($E_{1/2}$) of **AQ-1,8-3E-OH** is −0.43 V versus SHE at pH 7 and −0.52 V at pH 14 (Figure S6). The Pourbaix diagram in Figure 3b shows the pH dependence of its reduction potential; it is consistent with a transfer of 2 H$^+$/2 e^- from pH 5 to 10.8, 1 H$^+$/2 e^- from pH 10.8 to 12.6, and 0 H$^+$/2 e^- from pH 12.6 to 14. Similar pH-dependent behavior of the reduction potential has been observed for other anthraquinone derivatives in aqueous media (Figure S9).[18,34] Therefore, when starting at pH 7, the reduced **AQ-1,8-3E-OH** will exist in three different forms, as shown in Figure 3a. As its electrochemical reaction is pH-dependent and reversible, upon charging (reducing) the negolyte, a process that takes protons up from water, the pH of the initially neutral solution is expected to increase until it reaches approximately pK_{a2}. After discharging, a process that releases protons into the negolyte, the neutral pH is expected to be fully recovered.

Given the redox-activity and water-miscibility of **AQ-1,8-3E-OH** at pH 7, we investigated the performance of a PEGAQ-based flow cell with neutral electrolytes. To better understand the pH evolution during charge−discharge, we built a cell with 0.1 M electrolytes and tracked the pH of the negolyte during charge−discharge by immersing a pH probe in the negolyte (Figure 3c). To exclude the influence of oxygen dissolved in electrolytes on pH increase during charge, the electrolytes were first deaerated and then transferred to a glovebox filled with N_2.[14] In a full cycle with close to 100% Coulombic efficiency, the pH increased from 7 to 12.8 during charging and returned from pH 12.8 to 7 during discharging, confirming the pH reversibility. Compared to strongly acidic or basic electrolytes, such less-corrosive electrolytes (pH 7−13) are preferable in terms of less expensive electrolyte-contacting materials and structural stability of redox-active species.[6,11,14,35] On the basis of the Pourbaix diagram in Figure 3b, the absence of a visible signature of pH swing in the charge−discharge curves in Figure 3c seems surprising. This may occur because the local pH at the electrode surface can shift immediately upon the commencement of charging and discharging, while the bulk

DOI: 10.1021/acsenergylett.9b00739
ACS Energy Lett. 2019, 4, 1342−1348

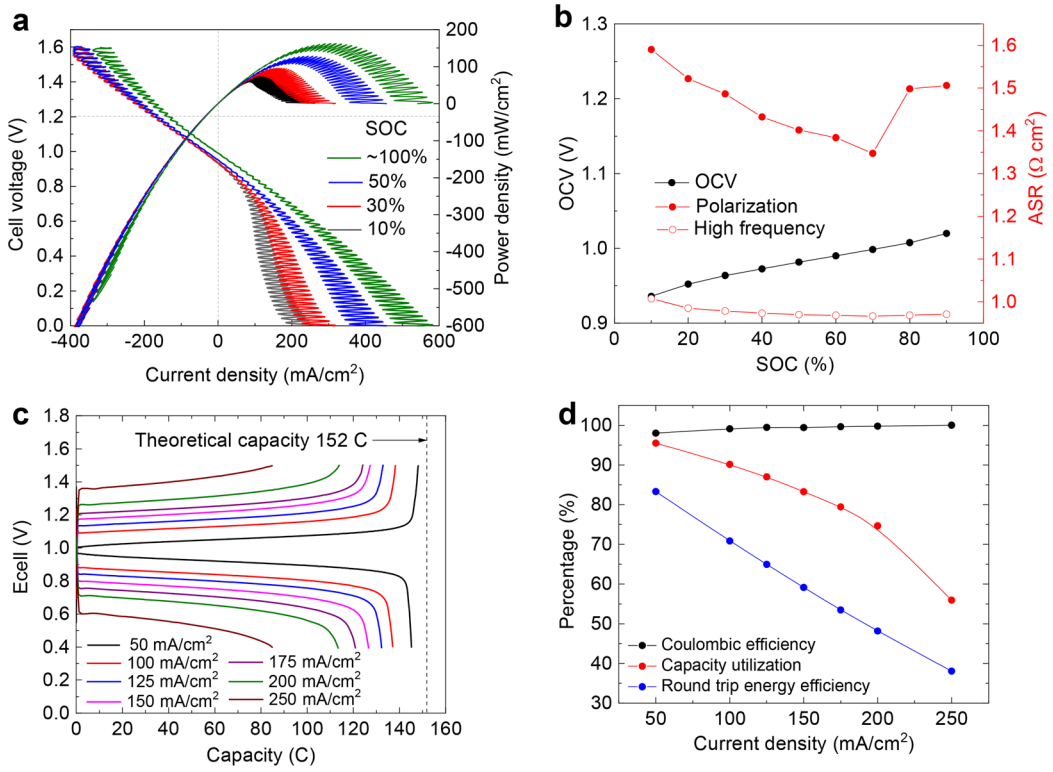

Figure 4. Low-concentration flow battery performance. (a) Cell voltage and power density versus current density at room temperature at 10%, 30%, 50%, and ~100% SOC. Electrolytes comprised 7.4 mL of 0.1 M AQ-1,8-3E-OH (negolyte) in 1 M KCl and 40 mL of 0.1 M potassium ferrocyanide and 0.04 M potassium ferricyanide (posolyte) in 1 M KCl. Current oscillations arise from peristaltic pumping. (b) OCV, high frequency, and polarization AC-ASR versus SOC. (c) Galvanostatic charge and discharge curves from 50 to 250 mA/cm² with 1.5 and 0.4 V cutoffs. The theoretical capacity is indicated by the vertical dashed line. (d) Coulombic efficiency, round-trip energy efficiency, and capacity utilization as a percentage of theoretical capacity versus current density.

pH changes over the longer time scale of the reservoir SOC tracked in Figure 3c.

Polarization experiments were conducted at different SOC of the negolyte, and a peak power density of 0.18 W cm^{-2} was achieved at ~100% SOC (Figure 4a). The open-circuit voltage (OCV) increases from 0.94 to 1.01 V as the SOC increases from 10% to 90%, and the OCV at 50% SOC was 0.98 V (Figure 4b). The alternating current area-specific resistance (AC-ASR) of the cell was determined via high-frequency electrochemical impedance spectroscopy (EIS), and the value was slightly lower than 1 Ω cm^2 across all SOCs (Figure 4b). The polarization ASR was determined using the linear region within the voltage range 0.9−1.1 V and the current range −50 to 50 mA (Figure 4a,b). The membrane resistance contributes more than 70% of the AC-ASR of the entire cell. The capacity utilization decreased from 95% at 50 mA/cm^2 to 84 and 56% at 150 and 250 mA/cm^2, respectively (Figure 4c,d).

To exploit the water-miscibility of **AQ-1,8-3E-OH**, we constructed a full cell with a concentrated negolyte comprising 7 mL of 1.5 M **AQ-1,8-3E-OH** in 1 M KCl as the capacity-limiting side and posolyte comprising 150 mL of 0.31 M $K_4Fe(CN)_6$ with 0.31 M $K_3Fe(CN)_6$ in 1 M KCl as the noncapacity-limiting side. In Figure 5, we demonstrate a negolyte with the record volumetric capacity of 80.4 Ah/L. Furthermore, **AQ-1,8-3E-OH** becomes a liquid when the temperature exceeds 35 °C, in which case the theoretical limit of the volumetric capacity is 120.1 Ah/L, corresponding to pure **AQ-1,8-3E-OH** (molarity: 2.24 M); in practice, however, the capacity of a real cell would be limited by the addition of water and salt for conductivity. Polarization experiments were further conducted, and the cell showed a higher OCV across all SOCs than with the previous 0.1 M-negolyte cell (1.06 V at 50% SOC, Figure 5a,b); this difference is explained in the Supporting Information (p 16). The high-frequency ASR in the high-concentration cell (Figure 5b) is approximately 1.3 times that of the low-concentration cell; we attribute this to the increased negolyte viscosity. **AQ-1,8-3E-OH** at 1.5 M possesses a viscosity of ~90 mPa·s at 37 °C, whereas the viscosity of a 0.1 M solution is only ~1 mPa·s (Figures S4 and S5). The higher viscosity slows the mass-transfer rate. Interestingly, an increase in viscosity of nearly 2 orders of magnitude does not incur proportional increases in either resistance or peak power density because of the countervailing influence of a 20-fold increase in negolyte reactant concentration. The peak power density of 0.17 W/cm^2 achieved at ~100% SOC in the high-concentration cell (Figure 5a) is only slightly lower than that in the low-concentration cell. In contrast, lower capacity utilization was observed when the high-concentration cell was charged and discharged at varying current densities. The accessible capacity at 50 mA/cm^2 was only 84.7% in the high-concentration cell (Figure S10), as a result of high-viscosity induced mass-transport limitations,[36,37] as opposed to 96% in the low-concentration (0.1 M) cell. A higher viscosity would lead to increased pumping power losses for a given flow channel configuration and electrode porosity and thickness, but these parameters would be chosen differently for low- and high-viscosity electrolytes.[38,39]

DOI: 10.1021/acsenergylett.9b00739
ACS Energy Lett. 2019, 4, 1342−1348

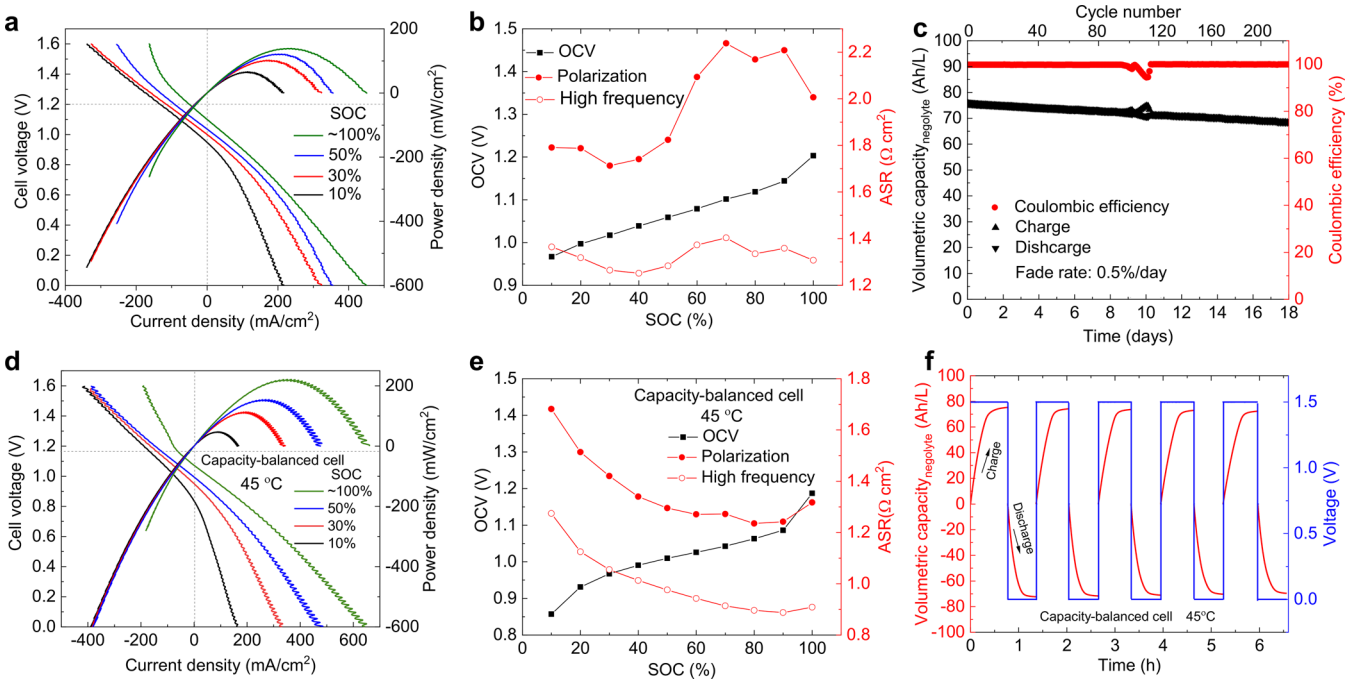

Figure 5. High-concentration flow cell performance. (a) Cell voltage and power density versus current density at room temperature at 10%, 30%, 50%, and ~100% SOC. Electrolytes comprised 7 mL of 1.5 M AQ-1,8-3E-OH (negolyte) in 1 M KCl and 150 mL of 0.31 M potassium ferrocyanide and 0.31 M potassium ferricyanide (posolyte) in 1 M KCl. (b) OCV, high frequency, and polarization ASR versus SOC. (c) Current efficiency and charge−discharge capacities versus time and cycle number. (d) Cell voltage and power density versus current density at 45 °C at 10%, 30%, 50%, and ~100% SOC. Electrolytes comprised 6 mL of 1.5 M AQ-1,8-3E-OH (negolyte) in 0.5 M KCl and 12 mL of 1.51 M 1:1 mixed potassium/sodium ferrocyanide and 0.01 M potassium ferricyanide (posolyte) in DI water. (e) OCV, high frequency, and polarization ASR versus SOC. (f) Charge−discharge under potentiostatic conditions.

Continuing to use the aforementioned cell setup and electrolytes, we performed a cycling experiment to evaluate the capacity fade rate by utilizing a sequential potential step method (Supporting Information, Full Cell Measurements, p 14). With this method, we accessed 95.7% of the theoretical capacity; the unutilized capacity might have been caused by a droplet electrolyte sticking on the wall of the electrolyte Falcon tube container or by a small amount of impurity in the sample. The achieved capacity utilization is comparable with that of prior work.[12,15] The cell was run for 220 cycles over 18 days with an average current efficiency of 99.90% (Figure 5c). The current efficiency decreased to 97% from the 105th to the 120th cycle because of depletion of nitrogen gas in the glovebag but then increased to >99.95% when the nitrogen supply was refilled. Apparently, such a disturbance does not influence the capacity fade rate, as the reaction with atmospheric oxygen is apparently self-discharge and not decomposition. We then fitted the capacity fade rate by using a first-order exponential decay model to obtain a temporal fade rate constant of 0.5%/day or 0.043%/cycle. As the capacity of the posolyte is 2.2 times that of the negolyte, and the negolyte crossover rate is negligible according to our permeability measurements,[11] we attribute the capacity fade exclusively to the decomposition of the active material in the negolyte. The decomposition product was identified, and possible decomposition pathways are proposed in the Supporting Information (Decomposition Analysis, pp 17−27, Figures S11−S18).

We investigated increasing the energy density by pairing the 1.5 M negolyte with a more concentrated posolyte. Mixing potassium and sodium ferrocyanides in a 1:1 molar ratio,[40] we were able to construct a capacity-balanced flow cell with 12 mL 1.51 M 1:1 mixed potassium/sodium ferrocyanide and 0.01 M potassium ferricyanide as the posolyte, and 6 mL 1.5 M **AQ-1,8-3E-OH** in 0.5 M KCl solution as the negolyte. The electrolyte reservoirs were immersed in a water bath and heated to 45 °C to prevent ferrocyanide precipitation. Polarization shows that the OCV at 50% SOC for this cell is 1.01 V (Figure 5e). Under elevated temperature, both high-frequency and polarization resistance are reduced significantly because of increased ion conductivity and reduced electrolyte viscosity. The peak power density of 0.22 W/cm², achieved at ~100% SOC, represents an approximately 30% increase compared to room-temperature performance. Using potentiostatic methods, charging at 1.5 V and discharging at 0 V, the cell accessed 94% of the theoretical capacity, which implies an energy density of 25.2 Wh/L—one of the highest among all organic aqueous and nonaqueous flow batteries. Theoretically, if 2.2 M **AQ-1,8-3E-OH** were paired with capacity-balanced 1.5 M ferrocyanide,[13,40] an energy density of 30.0 Wh/L would be expected.

In summary, we introduce **AQ-1,8-3E-OH** as the first water-miscible negolyte molecule for ARFBs. We demonstrate the highest volumetric capacity (80.4 Ah/L) ever reported among all aqueous organic electrolytes. The theoretical capacity limit is 120.1 Ah/L for the neat 2.2 M liquid quinone. An energy density of 25.2 Wh/L was demonstrated when 1.5 M **AQ-1,8-3E-OH** was paired with 1.5 M ferrocyanide. The theoretical energy density is 30.0 Wh/L for a full cell with a 2.2 M negolyte and a capacity-balanced 1.5 M ferrocyanide posolyte. As a first step toward developing lifetime extension strategies, post-mortem chemical analysis enabled us to identify the structure of a decomposition product and to propose four plausible degradation pathways. Further systematic exploration

DOI: 10.1021/acsenergylett.9b00739
ACS Energy Lett. 2019, 4, 1342−1348

of PEG functionalizations may shed light on the development of low-cost, high-capacity, and high-stability RAMs for ARFBs.

■ ASSOCIATED CONTENT

Supporting Information

The Supporting Information is available free of charge on the ACS Publications website at DOI: 10.1021/acsenergylett.9b00739.

Table of recent aqueous and nonaqueous flow battery works, synthesis, characterization, screening of PEGAQs, solubility measurements, electrochemical analysis, decomposition products analysis, and materials and methods (PDF)

■ AUTHOR INFORMATION

Corresponding Authors

*E-mail: gordon@chemistry.harvard.edu (R.G.G.).
*E-mail: maziz@harvard.edu (M.J.A.).

ORCID

Yan Jing: 0000-0002-5669-4609
Liuchuan Tong: 0000-0001-6211-6322
Daniel A. Pollack: 0000-0003-3909-5118
Roy G. Gordon: 0000-0001-5980-268X
Michael J. Aziz: 0000-0001-9657-9456

Present Address

§D.G.K.: Department of Mechanical Engineering, University of Michigan, Ann Arbor, MI 48109.

Author Contributions

∇S.J. and Y.J. contributed equally.

Notes

The authors declare no competing financial interest.

■ ACKNOWLEDGMENTS

This research was supported by U.S. DOE Award DE-AC05-76RL01830 through PNNL subcontract 428977, by ARPA-E Award DE-AR0000767, and by the Massachusetts Clean Energy Technology Center. We thank Prof. Luke Davis, Emily Kerr, Min Wu, Andrew Wong, Eric Fell, Winston Michalak, and James Niffenegger for useful discussions. D.A.P. acknowledges funding support from the NSF Graduate Research Fellowship Program, nos. DGE1144152 and DGE1745303.

■ REFERENCES

(1) Moya, A. A. Electric Circuits Modelling the Low-frequency Impedance of Ideal Ion-exchange Membrane Systems. *Electrochim. Acta* **2012**, *62*, 296−304.
(2) Rugolo, J.; Aziz, M. J. Electricity Storage for Intermittent Renewable Sources. *Energy Environ. Sci.* **2012**, *5*, 7151.
(3) Dunn, B.; Kamath, H.; Tarascon, J.-M. Electrical Energy Storage for the Grid: A Battery of Choices. *Science* **2011**, *334*, 928.
(4) Plesset, M. S.; Helfferich, F.; Franklin, J. N. Ion Exchange Kinetics. A Nonlinear Diffusion Problem. II. Particle Diffusion Controlled Exchange of Univalent and Bivalent Ions. *J. Chem. Phys.* **1958**, *29* (5), 1064−1069.
(5) Liu, W.; Lu, W.; Zhang, H.; Li, X. Aqueous Flow Batteries: Research and Development. *Chem. - Eur. J.* **2019**, *25*, 1649.
(6) Soloveichik, G. L. Flow Batteries: Current Status and Trends. *Chem. Rev.* **2015**, *115* (20), 11533−58.
(7) Li, L.; Kim, S.; Wang, W.; Vijayakumar, M.; Nie, Z.; Chen, B.; Zhang, J.; Xia, G.; Hu, J.; Graff, G.; Liu, J.; Yang, Z. A Stable Vanadium Redox-Flow Battery with High Energy Density for Large-Scale Energy Storage. *Adv. Energy Mater.* **2011**, *1*, 394.
(8) Bauer, F.; Denneler, S.; Willert-Porada, M. Influence of Temperature and Humidity on the Mechanical Properties of Nafion® 117 Polymer Electrolyte Membrane. *J. Polym. Sci., Part B: Polym. Phys.* **2005**, *43* (7), 786−795.
(9) Yang, Z.; Tong, L.; Tabor, D. P.; Beh, E. S.; Goulet, M.-A.; Porcellinis, D. D.; Aspuru-Guzik, A.; Gordon, R. G.; Aziz, M. J. Alkaline Benzoquinone Aqueous Flow Battery for Large-Scale Storage of Electrical Energy. *Adv. Energy Mater.* **2018**, *8*, 1702056.
(10) Dieterich, V. M.; Milshtein, J. D.; Barton, J. L.; Carney, T. J.; Darling, R. M.; Brushett, F. R. Estimating the Cost of Organic Battery Active Materials: A Case Study on Anthraquinone Disulfonic Acid. *Transl. Mater. Res.* **2018**, *5*, 034001.
(11) Kwabi, D. G.; Lin, K.; Ji, Y.; Kerr, E. F.; Goulet, M.-A.; Porcellinis, D. D.; Tabor, D. P.; Pollack, D. A.; Aspuru-Guzik, A.; Gordon, R. G.; Aziz, M. J. Alkaline Quinone Flow Battery with Long Lifetime at pH 12. *Joule* **2018**, *2* (9), 1907.
(12) Beh, E. S.; De Porcellinis, D.; Gracia, R. L.; Xia, K. T.; Gordon, R. G.; Aziz, M. J. A Neutral pH Aqueous Organic−Organometallic Redox Flow Battery with Extremely High Capacity Retention. *ACS Energy Lett.* **2017**, *2* (3), 639−644.
(13) Luo, J.; Hu, B.; Debruler, C.; Bi, Y.; Zhao, Y.; Bing, Y.; Hu, M.; Wu, W.; Liu, T. L. Unprecedented Capacity and Stability of Ammonium Ferrocyanide Catholyte in pH Neutral Aqueous Redox Flow Batteries. *Joule* **2019**, *3*, 149−163.
(14) Ji, Y.; Goulet, M.-A.; Pollack, D. A.; Kwabi, D. G.; Jin, S.; De Porcellinis, D.; Kerr, E. F.; Gordon, R. G.; Aziz, M. J. A Phosphonate-Functionalized Quinone Redox Flow Battery at Near-Neutral pH with Record Capacity Retention Rate. *Adv. Energy Mater.* **2019**, *9*, 1900039.
(15) Hollas, A.; Wei, X.; Murugesan, V.; Nie, Z.; Li, B.; Reed, D.; Liu, J.; Sprenkle, V.; Wang, W. A Biomimetic High-Capacity Phenazine-Based Anolyte for Aqueous Organic Redox Flow Batteries. *Nature Energy* **2018**, *3* (6), 508−514.
(16) Dominijanni, A.; Manassero, M. Modelling the Swelling and Osmotic Properties of Clay Soils. Part II: The Physical Approach. *Int. J. Eng. Sci.* **2012**, *51*, 51−73.
(17) DeBruler, C.; Hu, B.; Moss, J.; Luo, J.; Liu, T. L. A Sulfonate-Functionalized Viologen Enabling Neutral Cation Exchange, Aqueous Organic Redox Flow Batteries Toward Renewable Energy Storage. *ACS Energy Lett.* **2018**, *3* (3), 663−668.
(18) Huskinson, B.; Marshak, M. P.; Suh, C.; Er, S.; Gerhardt, M. R.; Galvin, C. J.; Chen, X.; Aspuru-Guzik, A.; Gordon, R. G.; Aziz, M. J. A Metal-free Organic-Inorganic Aqueous Flow Battery. *Nature* **2014**, *505* (7482), 195−8.
(19) Kusoglu, A.; Santare, M. H.; Karlsson, A. M. Mechanics-based Model for Non-affine Swelling in Perfluorosulfonic Acid (PFSA) Membranes. *Polymer* **2009**, *50* (11), 2481−2491.
(20) Janoschka, T.; Martin, N.; Hager, M. D.; Schubert, U. S. An Aqueous Redox-Flow Battery with High Capacity and Power: The TEMPTMA/MV System. *Angew. Chem., Int. Ed.* **2016**, *55* (46), 14427−14430.
(21) Wang, C.; Yang, Z.; Wang, Y.; Zhao, P.; Yan, W.; Zhu, G.; Ma, L.; Wang, L.; Li, G.; Liu, J.; Jin, Z. High-performance Alkaline Organic Redox Flow Batteries Based on 2-hydroxy-3-carboxy-1,4-naphthoquinone. *ACS Energy Lett.* **2018**, *3*, 2404.
(22) Lin, K.; Chen, Q.; Gerhardt, M. R.; Tong, L.; Kim, S. B.; Eisenach, L.; Valle, A. W.; Hardee, D.; Gordon, R. G.; Aziz, M. J.; Marshak, M. P. Alkaline Quinone Flow Battery. *Science* **2015**, *349* (6255), 1529.
(23) Lin, K.; Gómez-Bombarelli, R.; Beh, E. S.; Tong, L.; Chen, Q.; Valle, A.; Aspuru-Guzik, A.; Aziz, M. J.; Gordon, R. G. A Redox-flow Battery with an Alloxazine-based Organic Electrolyte. *Nature Energy* **2016**, *1* (9), 16102.
(24) Suttil, J. A.; Kucharyson, J. F.; Escalante-Garcia, I. L.; Cabrera, P. J.; James, B. R.; Savinell, R. F.; Sanford, M. S.; Thompson, L. T. Metal Acetylacetonate Complexes for High Energy Density Non-

DOI: 10.1021/acsenergylett.9b00739
ACS Energy Lett. 2019, 4, 1342−1348

aqueous Redox Flow Batteries. *J. Mater. Chem. A* **2015**, *3* (15), 7929−7938.
(25) Kwon, G.; Lee, S.; Hwang, J.; Shim, H.-S.; Lee, B.; Lee, M. H.; Ko, Y.; Jung, S.-K.; Ku, K.; Hong, J.; Kang, K. Multi-redox Molecule for High-Energy Redox Flow Batteries. *Joule* **2018**, *2*, 1771−1782.
(26) Hu, B.; Liu, T. L. Two Electron Utilization of Methyl Viologen Anolyte in Nonaqueous Organic Redox Flow Battery. *J. Energy Chem.* **2018**, *27* (5), 1326−1332.
(27) Yang, B.; Hoober-Burkhardt, L.; Wang, F.; Surya Prakash, G. K.; Narayanan, S. R. An Inexpensive Aqueous Flow Battery for Large-scale Electrical Energy Storage Based on Water-soluble Organic Redox Couples. *J. Electrochem. Soc.* **2014**, *161*, A1371−A1380.
(28) Wei, X.; Duan, W.; Huang, J.; Zhang, L.; Li, B.; Reed, D.; Xu, W.; Sprenkle, V.; Wang, W. A High-current, Stable Nonaqueous Organic Redox Flow Battery. *ACS Energy Letters* **2016**, *1* (4), 705−711.
(29) Hu, B.; DeBruler, C.; Rhodes, Z.; Liu, T. Leo Long-cycling Aqueous Organic Redox Flow Battery (AORFB) Toward Sustainable and Safe Energy Storage. *J. Am. Chem. Soc.* **2017**, *139* (3), 1207−1214.
(30) Wei, X.; Xu, W.; Huang, J.; Zhang, L.; Walter, E.; Lawrence, C.; Vijayakumar, M.; Henderson, W. A.; Liu, T.; Cosimbescu, L.; Li, B.; Sprenkle, V.; Wang, W. Radical Compatibility with Nonaqueous Electrolytes and Its Impact on an All-organic Redox Flow Battery. *Angew. Chem., Int. Ed.* **2015**, *54* (30), 8684−7.
(31) Huskinson, B.; Marshak, M. P.; Gerhardt, M. R.; Aziz, M. J. Cycling of a Quinone-Bromide Flow Battery for Large-Scale Electrochemical Energy Storage. *ECS Trans.* **2014**, *61* (37), 27−30.
(32) Ponce de León, C.; Frías-Ferrer, A.; González-García, J.; Szánto, D. A.; Walsh, F. C. Redox Flow Cells for Energy Conversion. *J. Power Sources* **2006**, *160* (1), 716−732.
(33) Giguere, J. B.; Morin, J. F. New Strapped Porphyrins as Hosts for Fullerenes: Synthesis and Complexation Study. *Org. Biomol. Chem.* **2012**, *10* (5), 1047−51.
(34) Quan, M.; Sanchez, D.; Wasylkiw, M. F.; Smith, D. K. Voltammetry of Quinones in Unbuffered Aqueous Solution: Reassessing the Roles of Proton Transfer and Hydrogen Bonding in the Aqueous Electrochemistry of Quinones. *J. Am. Chem. Soc.* **2007**, *129*, 12847−12856.
(35) Silberstein, M. N.; Boyce, M. C. Constitutive Modeling of the Rate, Temperature, and Hydration Dependent Deformation Response of Nafion to Monotonic and Cyclic Loading. *J. Power Sources* **2010**, *195* (17), 5692−5706.
(36) Chen, Q.; Gerhardt, M. R.; Aziz, M. J. Dissection of the Voltage Losses of an Acidic Quinone Redox Flow Battery. *J. Electrochem. Soc.* **2017**, *164* (6), A1126−A1132.
(37) Milshtein, J. D.; Tenny, K. M.; Barton, J. L.; Drake, J.; Darling, R. M.; Brushett, F. R. Quantifying Mass Transfer Rates in Redox Flow Batteries. *J. Electrochem. Soc.* **2017**, *164*, E3265−E3275.
(38) Milshtein, J. D.; Darling, R. M.; Drake, J.; Perry, M. L.; Brushett, F. R. The Critical Role of Supporting Electrolyte Selection on Flow Battery Cost. *J. Electrochem. Soc.* **2017**, *164* (14), A3883−A3895.
(39) Gerhardt, M. R.; Wong, A. A.; Aziz, M. J. The Effect of Interdigitated Channel and Land Dimensions on Flow Cell Performance. *J. Electrochem. Soc.* **2018**, *165* (11), A2625−A2643.
(40) Nemat-Nasser, S. Micromechanics of Actuation of Ionic Polymer-Metal Composites. *J. Appl. Phys.* **2002**, *92* (5), 2899−2915.

DOI: 10.1021/acsenergylett.9b00739
ACS Energy Lett. 2019, 4, 1342−1348

Electronic Supplementary Information

A Water-Miscible Quinone Flow Battery with High Volumetric Capacity and Energy Density

Shijian Jin,[▽,†] Yan Jing,[▽,‡] David G. Kwabi,[†,§] Yunlong Ji,[‡] Liuchuan Tong,[‡] Diana De Porcellinis,[†] Marc-Antoni Goulet,[†] Daniel A. Pollack,[#] Roy G. Gordon,[†,‡,] and Michael J. Aziz[†,*]*

[▽] Shijian Jin and Yan Jing contributed equally.

† John A. Paulson School of Engineering and Applied Sciences, Harvard University, Cambridge, MA 02138, USA

‡ Department of Chemistry and Chemical Biology, Harvard University, Cambridge, MA 02138, USA

§ Present Address: Department of Mechanical Engineering, University of Michigan, Ann Arbor, MI 48109

Department of Physics, Harvard University, Cambridge, MA 02138, USA

* To whom correspondence should be addressed: gordon@chemistry.harvard.edu (Roy G. Gordon); maziz@harvard.edu (Michael J. Aziz).

Table S1. Summary of demonstrated cell capacity and energy density of existing flow batteries in Figure 2b.

No./ Ref. in the plot	Negolyte/ electrons	Conc. of negolyte (M)	Posolyte/ electrons	Conc. of posolyte (M)	Volt. at 50% SOC (V)	Demonstrated cell capacity (Ah/L)*	Demonstrated cell energy density (Wh/L)
1/[1]	$V(acac)_3$/1	0.1	$V(acac)_3$/1	0.1	2.1	1.34	2.81
2/[2]	FL/1	0.1	DMPZ/2	0.05	1.6	1.34	2.14
3/[3]	MVTFSI/2	0.1	FcNTFSI/1	0.2	1.2	2.68	3.22
4/[4]	DPPEAQ/2	0.5	$K_4Fe(CN)_6$/1	0.4	1.0	1.58	1.58
5/[5]	DBEAQ/2	0.5	$K_4Fe(CN)_6$/1	0.3	1.05	2.49	2.61
6/[6]	AQS/2	0.2	BQDS/2	0.2	0.76	5.36	4.07
7/[7]	MePh/1	0.3	DBMMB/1	0.3	2.3	3.2	7.36
8/[8]	DHPS/2	1.4	$K_4Fe(CN)_6$/1	0.31	1.4	6.75	9.46
9/[9]	DHAQ/2	0.5	$K_4Fe(CN)_6$/1	0.4	1.2	6.7	8.04
10/[10]	DHBQ/2	0.5	$K_4Fe(CN)_6$/1	0.4	1.21	4.85	5.87
11/[11]	ACA/2	1	$K_4Fe(CN)_6$/1	0.4	1.15	6.31	7.25
12/[12]	methyl-Vi/1	0.5	FcNCl/1	0.5	1.05	6.70	7.04
13/[13]	FL/1	0.5	DBMMB/1	0.5	2.37	5.80	11.41
14/[14]	$(SPr)_2$Vi/1	0.9	$NH_4Fe(CN)_6$/1	0.9	0.82	12.06	9.89
15/[15]	BTMAP-Vi/1	1.3	BTMAP-Fc/1	1.3	0.7	15.20	10.64
16/[16]	AQDS/2	1	HBr/1	3	0.8	24.36	19.49
17/[17]	vanadium/1	1.5†	Vanadium/1	1.5	1.25	20.10	25.13
18/[18]	methyl -Vi/1	2	TEMPTMA/1	2	1.2	22.5	27.00
19	PEGAQ/2	1.5	$Na_4/K_4Fe(CN)_6$/1	1.51	1.05	25.20	25.45
20/[19]	vanadium/1	2.5†	Vanadium/1	2.5†	1.25	33.50	41.88

*Demonstrated cell capacity is calculated by $(C_{CLS}/V_{tot})\times\Phi$, where C_{CLS} is the capacity of the capacity limiting side, V_{tot} is the volume of posolyte plus the volume of negolyte, and Φ is the utilized capacity as a percentage. † 1.5 M solubility of vanadium species was achieved by using 2.5 M H_2SO_4 as the supporting electrolyte, while 2.5 M solubility of vanadium species was achieved by using a mixture of 2.5 M H_2SO_4 and 6 M HCl as the supporting electrolyte.

Table S2. List of chemicals and their abbreviations.

Abbreviation	Full name
$(SPr)_2V$	1,10-bis(3-sulfonatopropyl)-4,40-bipyridinium
AQDS	9,10-dioxo-9,10-dihydroanthracene-2,6-disulfonic acid
AQS	anthraquinone-2-sulfonic acid
BQDS	1,2-benzoquinone- 3,5-disulfonic acid
BTMAP-Fc	bis((3-trimethylammonio)propyl)- ferrocene dichloride
BTMAP-Vi	bis(3-trimethylammonio)propyl viologen tetrachloride
DBEAQ	4,40-((9,10-Anthraquinone-2,6-diyl)dioxy)dibutyric Acid
DBMMB	,5-di-tert-butyl-1-methoxy-4-[2′ -methoxyethoxy]benzene
DHAQ	2,6-dihydroxy anthraquinone
DHBQ	2,5-dihydroxycyclohexa-2,5-diene-1,4-dione
DHPS	7,8-dihydroxyphenazine-2-sulfonic acid
DMPZ	5,10-dihydro-5,10-dimethyl phenazine
FcNCl	((ferrocenylmethyl)trimethylammonium choride
FcNTFSI	(ferrocenylmethyl)trimethylammonium bis(trifluoromethanesulfonyl)imide
FL	9-fluorenone
MePh	N-methylphthalimide
MV	methyl viologen
MViTFSI	methyl viologen bis(trifluoromethane)sulfonamide
TEMPTMA	N,N,N-2,2,6,6-heptamethylpiperidinyl oxy-4-ammonium chloride
$V(acac)_3$	vanadium (III) acetylacetonate

General Information

LC-MS was conducted on a Bruker microTOF-Q II mass spectrometer. All chemicals were purchased from Sigma-Aldrich unless specified otherwise. All dihydroxyanthraquinone (DHAQ) isomers, except the 2,6- and 2,7- isomers, were purchased from Alfa Aesar; 2,6-DHAQ was purchased from AK Scientific; and 2,7-DHAQ was synthesized from anthraquinone-2,7-disulfonic acid disodium salt[20], which was purchased from TCI America. All chemicals were used as received unless specified otherwise. Viscosity measurements were conducted on a Cambridge Viscosity VISCOlab3000 viscometer.

Synthesis and Chemical Characterization

The procedure is a modification of the method described in Giguere *et al.*[21]: *n, m*-dihydroxy-anthraquinone (DHAQ) (1 equiv.) was mixed with anhydrous K_2CO_3 (4 equiv.), NaI (0.15 equiv.), and 2-(2-(2-chloroethoxy)ethoxy)ethan-1-ol (3 equiv.) in DMF to achieve a 0.4 M DHAQ suspension in a pressure vessel. The reaction mixture was heated to 135 °C and stirred overnight. Water (2×DMF volume) was then added to the reaction mixture, which was subsequently extracted with DCM (2×DMF volume) three times. The organic layer was dried over Na_2SO_4 and then condensed under vacuum to achieve crude product. Silica gel column chromatography (eluent: 97 v/v% dichloromethane + 3 v/v% Methanol) was used to obtain the *n, m*-di-Pegylated-Anthraquinone.

(a) 1,2-bis(2-(2-(2-hydroxyethoxy)ethoxy)ethoxy)anthracene-9,10-dione

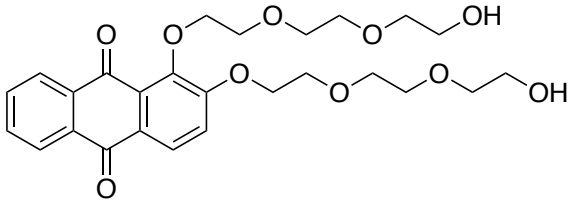

A purple solid was obtained after column chromatography. Final yield: 30.1%. ^{1}H NMR (500 MHz, $CDCl_3$) δ 8.22-8.26 (m, 2H), 8.13(d, J = 8.6 Hz, 1H), 7.73-7.76 (m, 2H), 7.26 (d, J = 8.6 Hz, 1H) , 4.27-4.35 (m, 4H), 4.02-4.07 (m, 2H), 3.94-3.98 (m, 2H), 3.79-3.83 (m, 2H), 3.75-3.79 (m, 2H), 3.66-3.75 (m, 8H), 3.57-3.64 (m, 4H). ^{13}C NMR (125 MHz, $CDCl_3$) δ 182.77, 182.46, 158.38, 148.97, 135.22, 133.99, 133.65, 133.06, 127.70, 127.25, 127.21, 126.80, 125.26, 117.45, 72.99, 72.83, 72.81, 71.03, 70.79, 70.69, 70.54, 70.52, 69.43, 68.79, 61.82, 61.78. MS (ESI m/z) calcd. for $[C_{26}H_{32}O_{10}+Na]^+$ 527.19, found 527.19.

(b) 1,4-bis(2-(2-(2-hydroxyethoxy)ethoxy)ethoxy)anthracene-9,10-dione

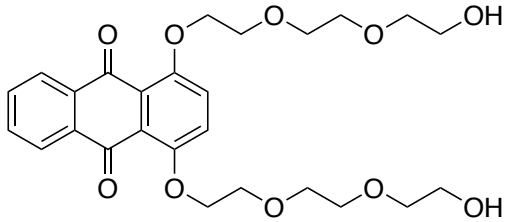

A yellow-brown mud was obtained after column chromatography. Final yield: 47.6%. ^{1}H NMR (500 MHz, $CDCl_3$) δ 8.09 (m, 2H), 7.66 (m, 2H), 7.34 (s, 2H), 4.23 (t, J = 4.9 Hz, 4H), 3.94 (t, J

= 3.9 Hz, 4H), 3.77-3.80 (m, 4H), 3.65-3.70 (m, 8H), 3.56-3.60 (m, 4H). ^{13}C NMR (125 MHz, $CDCl_3$) δ 183.18, 154.05, 134.30, 133.40, 126.50, 123.93, 123.39, 72.63, 71.14, 70.58, 70.56, 69.89, 61.88. MS (ESI m/z) calcd. for $[C_{26}H_{32}O_{10}+Na]^+$ 527.19, found 527.19.

(c) 1,5-bis(2-(2-(2-hydroxyethoxy)ethoxy)ethoxy)anthracene-9,10-dione

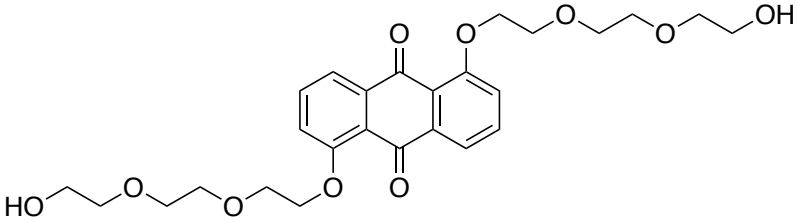

A golden solid was obtained after column chromatography. Final yield: 48.0%. ^{1}H NMR (500 MHz, $CDCl_3$) δ 7.89 (dd, J = 1.0, 7.8 Hz , 2H), 7.67 (t, J = 8.4, 2H) , 7.28 (dd, J = 1.0, 8.4 Hz, 2H), 4.32 (t, J = 4.7 Hz, 4H), 4.03 (t, J = 4.7 Hz, 4H), 3.85-3.90 (m, 4H), 3.70-3.75 (m, 8H), 3.61-3.66 (m, 4H), 2.00 (broad s, 2H). ^{13}C NMR (125 MHz, $CDCl_3$) δ 182.55, 159.12, 137.51, 135.05, 121.47, 120.19, 118.60, 72.63, 71.29, 70.62, 69.59, 69.57, 61.95. MS (ESI m/z) calcd. for $[C_{26}H_{32}O_{10}+Na]^+$ 527.19, found 527.19.

(d) 1,8-bis(2-(2-(2-hydroxyethoxy)ethoxy)ethoxy)anthracene-9,10-dione

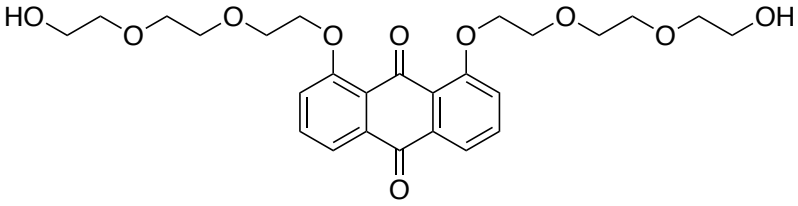

A brown-red mud was obtained after column chromatography. Final yield: 66.1%. ^{1}H NMR (500 MHz, $CDCl_3$) δ 7.85 (d, J = 7.7 Hz, 2H), 7.61 (t, J = 8.4 Hz, 2H), 7.32 (d, J = 8.4 Hz, 2H), 4.30 (t, J = 5.0 Hz, 4H), 4.01 (t, J =5.0 Hz, 4H), 3.85-3.90 (m, 4H), 3.69-3.74 (m, 8H), 3.60-3.54 (m, 4H), 2.52 (broad s, 2H). ^{13}C NMR (125 MHz, $CDCl_3$) δ 183.93, 182.42, 158.59, 134.87, 124.79, 120.23, 119.63, 72.77, 71.26, 70.59, 69.91, 69.62, 61.80. MS (ESI m/z) calcd. for $[C_{26}H_{32}O_{10}+Na]^+$ 527.19, found 527.19.

(e) 2,6-bis(2-(2-(2-hydroxyethoxy)ethoxy)ethoxy)anthracene-9,10-dione

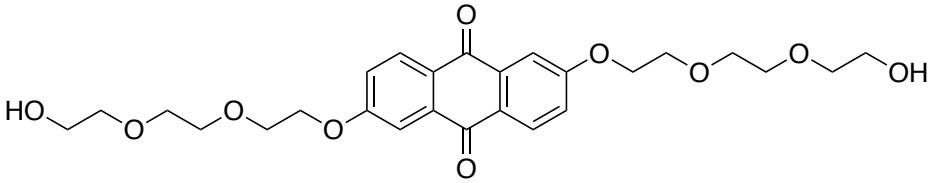

A yellow solid was obtained after column chromatography. Final yield: 75.0%. ^{1}H NMR (500 MHz, $CDCl_3$) δ 8.23 (d, J = 8.6 Hz, 2H), 7.73 (d, J = 2.7 Hz, 2H), 7.28 (dd, J = 2.7, 8.6 Hz, 2H), 4.33 (t, J = 4.75 Hz, 4H), 3.93 (t, J = 4.75 Hz, 4H), 3.70-3.78 (m, 16H), 3.41-3.61 (m, 4H). ^{13}C NMR (125 MHz, $CDCl_3$) δ 182.23, 163.71, 135.87, 129.81, 127.41, 121.29, 110.70, 72.63, 71.06, 70.52, 69.57, 68.18, 61.90. MS (ESI m/z) calcd. for $[C_{26}H_{32}O_{10}+Na]^+$ 527.19, found 527.19.

(f) 2,7-bis(2-(2-(2-hydroxyethoxy)ethoxy)ethoxy)anthracene-9,10-dione

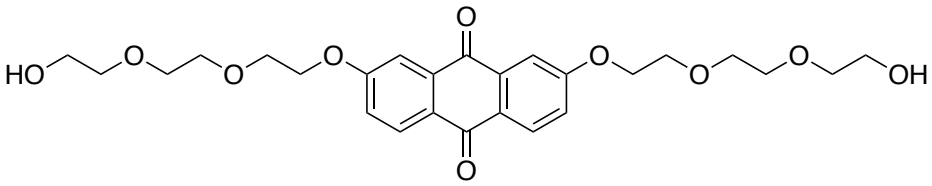

A yellow solid was obtained after column chromatography. Final yield: 60.3%. ^{1}H NMR (500 MHz, $CDCl_3$) δ 8.23 (d, J = 8.4 Hz, 2H), 7.71 (d, J = 3.0 Hz, 2H), 7.29 (dd, J = 3.0, 8.4 Hz, 2H), 4.33 (t, J = 4.8 Hz, 4H), 3.93 (t, 4.8Hz, 4H), 3.69-3.78 (m, 16H), 3.61-3.65(m, 16H), 2.33 (broad s, 2H). ^{13}C NMR (125 MHz, $CDCl_3$) δ 183.24, 181.29, 163.20, 135.54, 129.68, 127.38, 121.60, 110.70, 72.65, 71.00, 70.43, 69.51, 68.11, 61.81. MS (ESI m/z) calcd. for $[C_{26}H_{32}O_{10}+Na]^+$ 527.19, found 527.19.

(g) 1,8-bis(2-(2-(2-methoxyethoxy)ethoxy)ethoxy)anthracene-9,10-dione

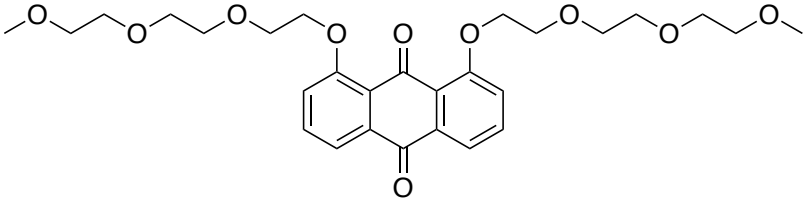

An orange oil was obtained after column chromatography. Final yield: 80.5%. ^{1}H NMR (600 MHz, $CDCl_3$) δ 7.82 (dd, J = 0.9, 7.7 Hz, 2H), 7.59 (d, J = 8.4 Hz, 2H), 7.34 (dd, J = 0.9, 8.4 Hz, 2H), 4.29 (t, J = 4.9 Hz, 4H), 3.96-3.99 (m, 4H), 3.81-3.84 (m, 4H), 3.66-3.68(m, 4H), 3.62-3.64(m, 4H), 3.51-3.53(m, 4H), 3.34 (s, 6H). ^{13}C NMR (150 MHz, $CDCl_3$) δ 184.06, 182.38, 158.72, 134.85, 133.84, 124.84, 120.56, 119.64, 72.00, 71.13, 70.82, 50.58, 69.81, 69.67, 59.10. MS (ESI m/z) calcd. for $[C_{28}H_{36}O_{10}+Na]^+$ 555.22, found 555.22.

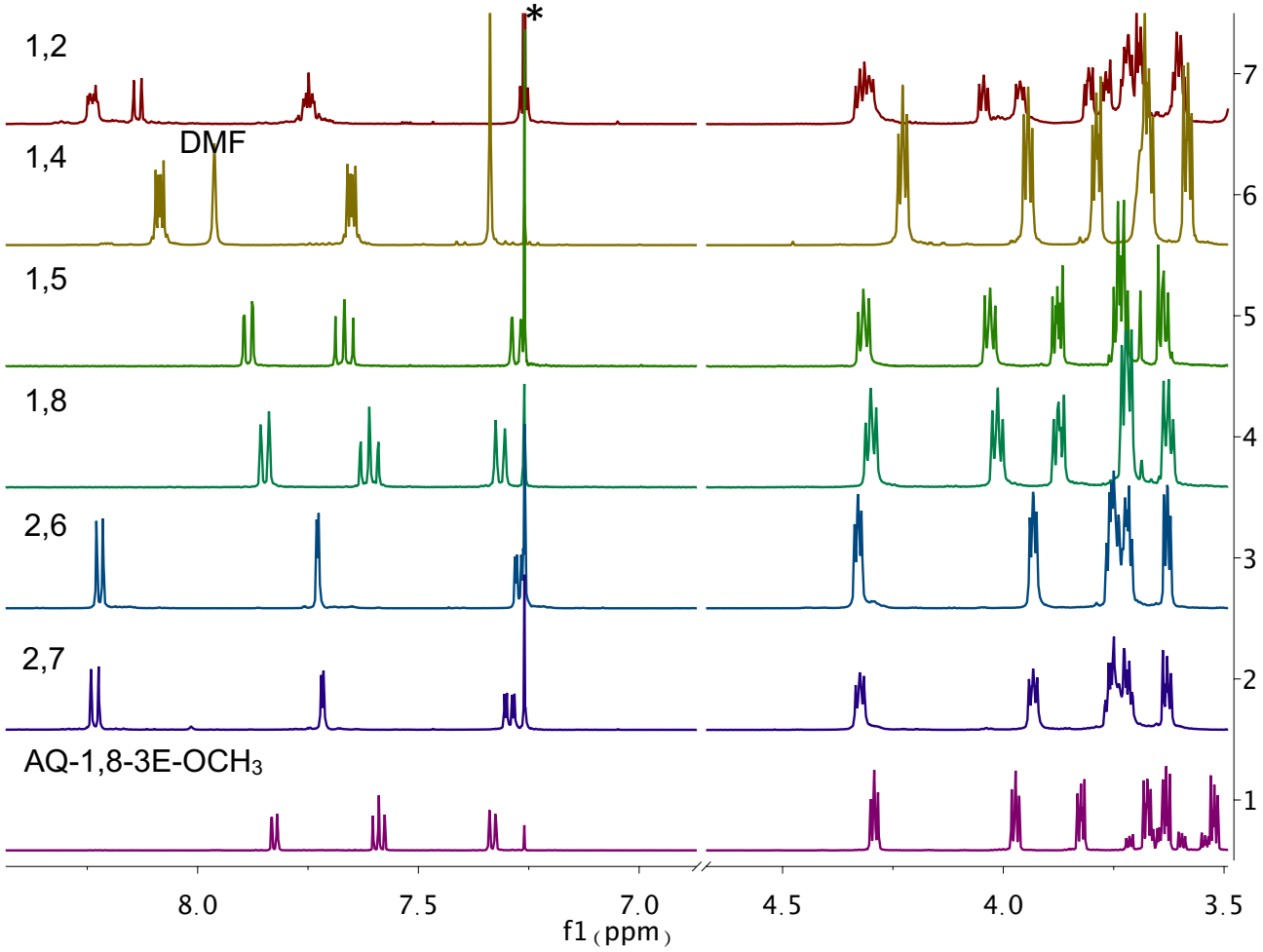

Figure S1. ^{1}H NMR spectra of 1,2-, 1,4-, 1,5-, 1,8-, 2,6-, 2,7-bis(2-(2-(2-hydroxyethoxy)ethoxy)ethoxy)anthracene-9,10-dione (AQ-*n,m*-3E-OH) and AQ-1,8-3E-OCH_3 in $CDCl_3$. The peak labeled with * is from a trace amount of $CHCl_3$ in $CDCl_3$ solvent at 7.26 ppm.

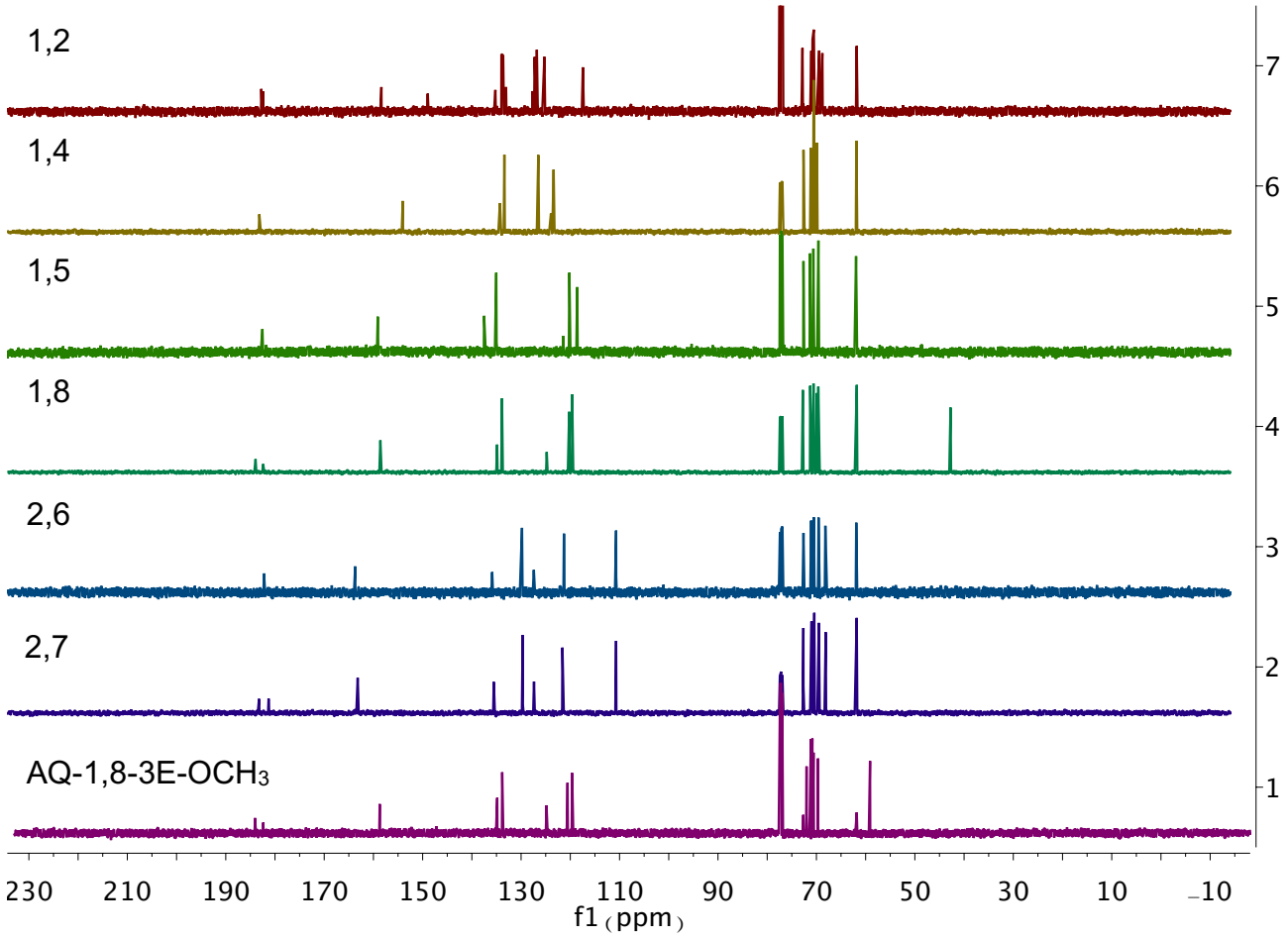

Figure S2. ^{13}C NMR spectra of 1,2-, 1,4-, 1,5-, 1,8-, 2,6-, 2,7-bis(2-(2-(2-hydroxyethoxy)ethoxy)ethoxy)anthracene-9,10-dione (AQ-*n,m*-3E-OH) and AQ-1,8-3E-OCH_3 in $CDCl_3$.

Solubility Measurements

The solubilities of the PEG-AQ isomers were measured by adding solids/liquids of pure AQ species into 1 M KCl solution until precipitate was observed, and the solubility was calculated using the mass of compound added and the final volume of the solution. Since the 1,8- and 1,4-isomers are miscible with water, the maximum concentration is obtained by calculating the density (ρ = 1.13 g/mL) divided by the molecular weight (504.53 g/mol), which gives 2.24 M as the maximum concentration. The theoretical maximal volumetric capacity (Ah/L) can be calculated by $n \times F \times C/3600$ (Ah/L), where n represents the number of electrons stored per AQ, F is Faraday's constant with units of Coulomb/mol, and C is the maximum concentration of AQ-1,8-3E-OH with units of M or mol/L (*e.g.*, 2.24 M). Theoretically, the maximal volumetric capacity is thus 120.1 Ah/L. Figure S4 depicts AQ-1,8-3E-OH at different concentrations.

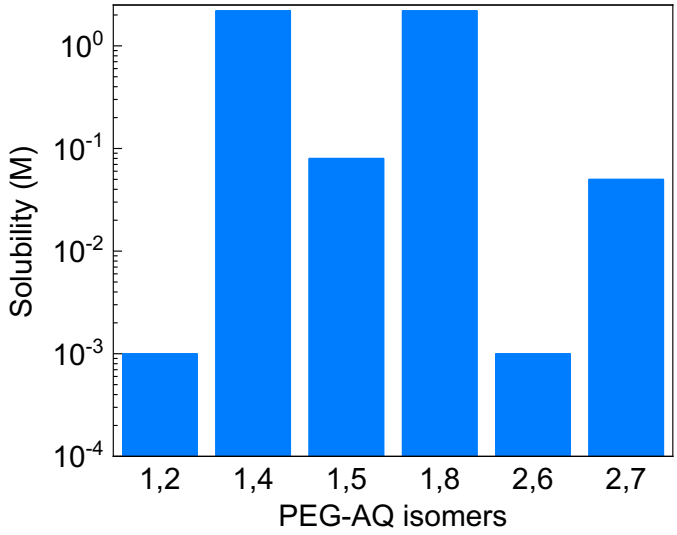

Figure S3. Measured solubility of PEGAQ isomers in 1 M KCl solution at neutral pH. The position of PEG chains tethered to AQ can influence final solubility by orders of magnitude. The 1,4- and 1,8- isomers are water-miscible; thus the bars indicate the concentrations of pure liquid PEG-AQ. The solubilities of the 1,5- and 2,7- isomers are ~0.1 M; and the solubilities of the 1,2- and 2,6- isomers are less than 1 mM.

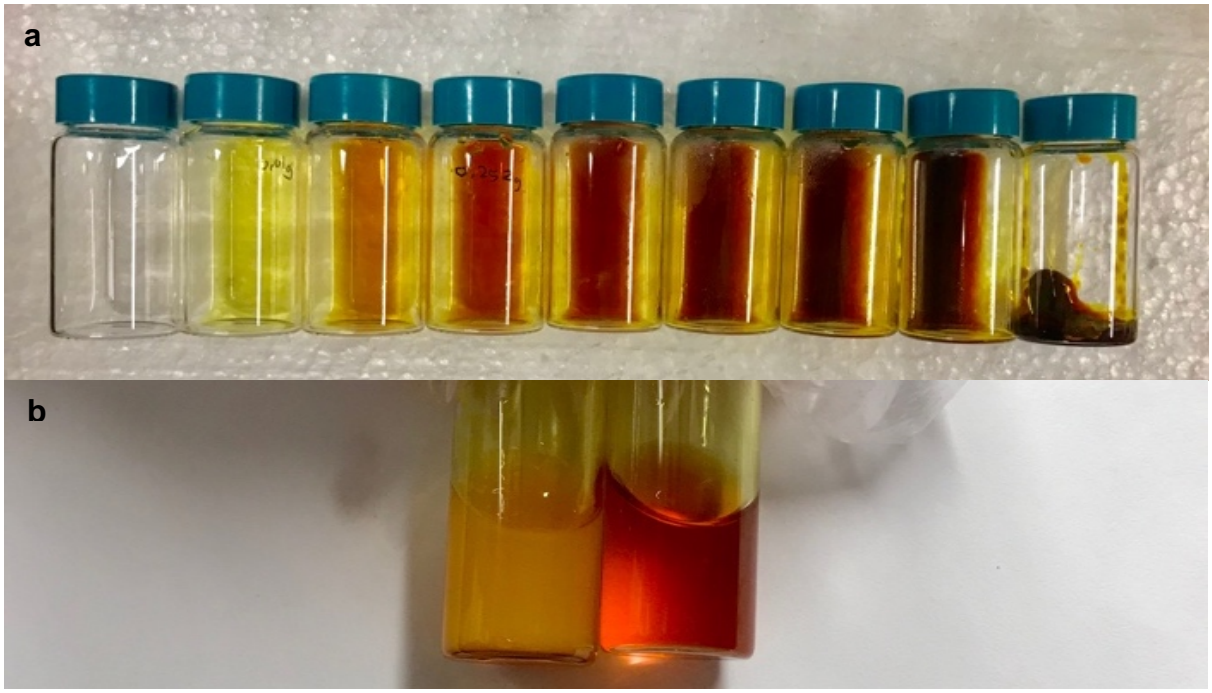

Figure S4. (a) Aqueous solutions with AQ-1,8-3E-OH at concentrations of (from left to right) 0, 0.01, 0.1, 0.25, 0.5, 0.75, 1.0, 1.5, and (pure compound) 2.24 M. Pure AQ-1,8-3E-OH melts above 35 ˚C. The viscosity of these solutions were measured. (b) Comparison of 0.1 M AQ-1,8-3E-OCH_3 (left) and AQ-1,8-3E-OH (right) in 1 M KCl solution at 45 °C. The AQ-1,8-3E-OCH_3 solution

becomes cloudy and phase-separated, while the AQ-1,8-3E-OH solution remains homogeneous and transparent.

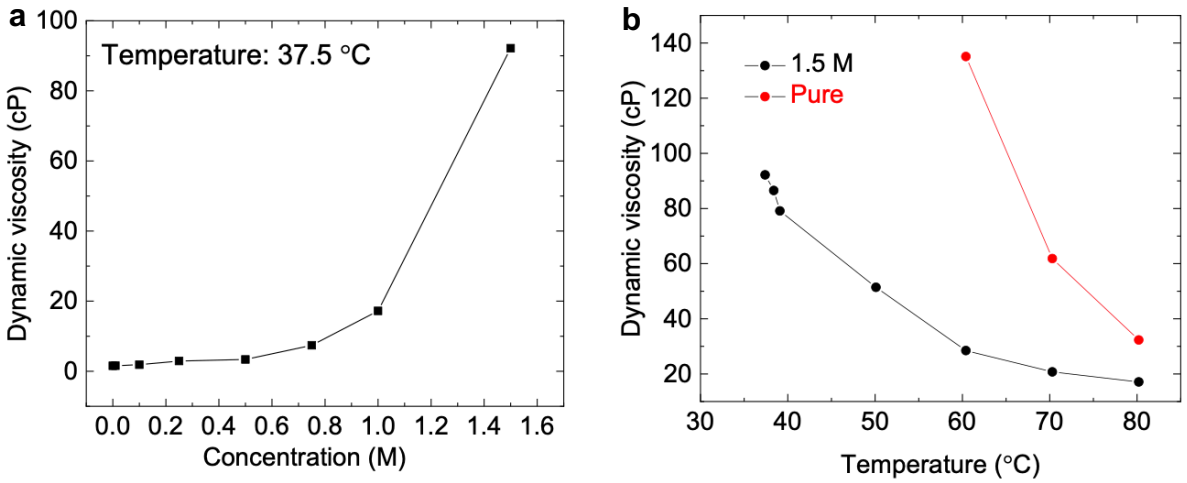

Figure S5. (a) Viscosity of AQ-1,8-3E-OH at concentrations of 0, 0.01, 0.1, 0.25, 0.5, 0.75, 1.0, and 1.5 M at 37.5±0.2 °C. (b) Viscosity of 1.5 M and pure AQ-1,8-3E-OH at different temperatures.

Electrochemical Characterization

Glassy carbon was used as the working electrode for all three-electrode CV tests. Rotating Disk Electrode experiments were conducted using a Pine Instruments Modulated Speed Rotator AFMSRCE equipped with a 5 mm diameter glassy carbon working electrode, a Ag/AgCl reference electrode (BASi, pre-soaked in 3 M NaCl solution), and a graphite counter electrode. The diffusion coefficient of the oxidized form of AQ-1,8-3E-OH was calculated using the Levich equation, which relates the mass-transport-limited current to the number of electrons transferred (n), the area of the electrode (A), and the concentration of redox-active species in the electrolyte (C), by plotting the mass-transport-limited current against the square root of the rotation rate (Figure S7) with the following parameters: n = 2, F = 96,485 Coulombs/mol, A = 0.196 cm^2, C = 5 mM, ν = 1.08 × 10^{-6} m^2/s (the kinematic viscosity of 1 M KCl)[22].The resulting value of the diffusion coefficient of AQ-1,8-3E-OH is 2.94 × 10^{-6} cm^2/s. Koutecký–Levich analysis at low overpotentials can be extrapolated to infinite rotation rate and fitted to the Butler-Volmer equation to give the kinetic reduction rate constant k_0 = 6.1(4) × 10^{-3} cm/s.

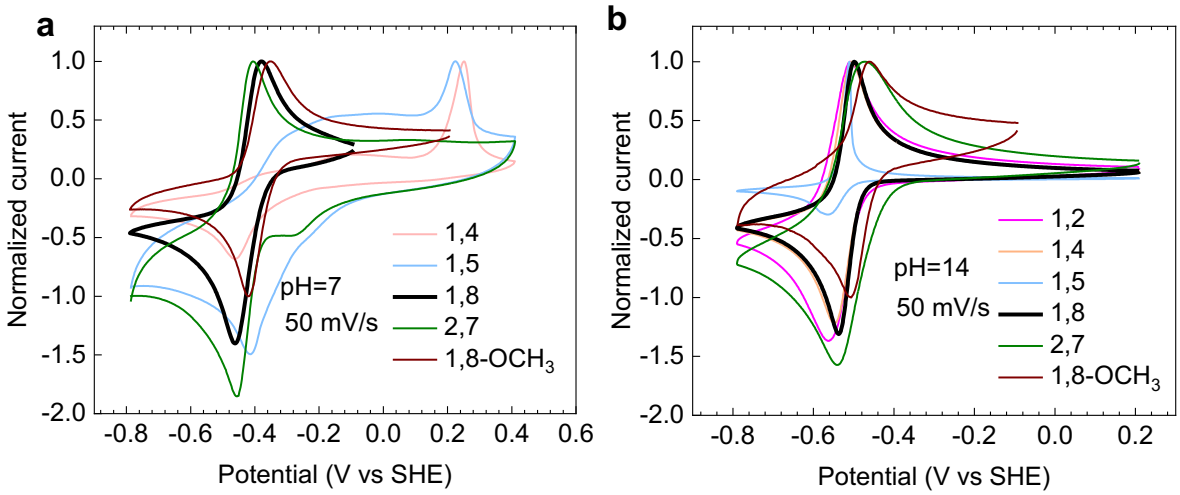

Figure S6. (a) CV of AQ- 1,4-, 1,5-, 1,8-, 2,7- 3E-OH and AQ-1,8-3E-OCH_3 in 1 M KCl measured with 50 mV/s scan rate and normalized to the height of the oxidative peak near 0.4 V. The 1,2- and 2,6- isomers were not soluble enough for CV measurements. The 1,8- and 2,7- isomers show reversible electrochemical behavior, while the 1,4- and 1,5- are irreversible. (b) CV of AQ- 1,2-, 1,4-, 1,5-, 1,8-, 2,7- 3E-OH and AQ-1,8-3E-OCH_3 in 1 M KOH measured with 50 mV/s scan rate and normalized to the height of the oxidative peak near 0.5 V. The 2,6- isomer is not soluble enough for CV measurements. All isomers except 1,5- showed reversible electrochemical behavior.

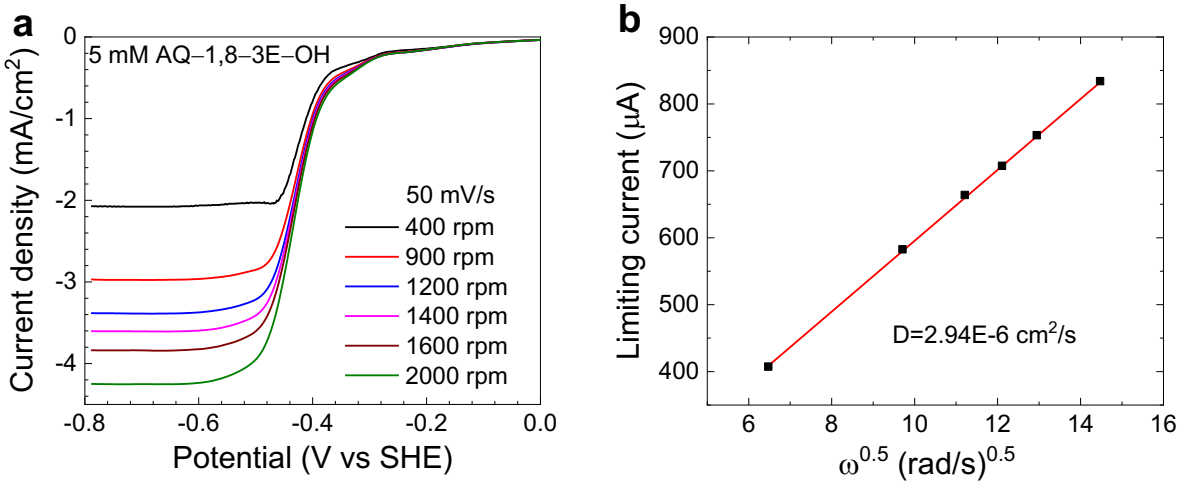

Figure S7. (a) RDE study of the reduction of 5 mM AQ-1,8-3E-OH in 1 M KCl on a glassy carbon electrode at rotation rates between 400 and 2000 rpm. (b) Levich plot (limiting current *vs.* square root of rotation rate in rad/s) of 5 mM AQ-1,8-3E-OH in 1 M KCl. Limiting current is taken as the current in the range –0.7 to –0.8 V in (a). The slope yields a diffusion coefficient for the oxidized form of AQ-1,8-3E-OH of 2.94×10^{-6} cm^2/s.

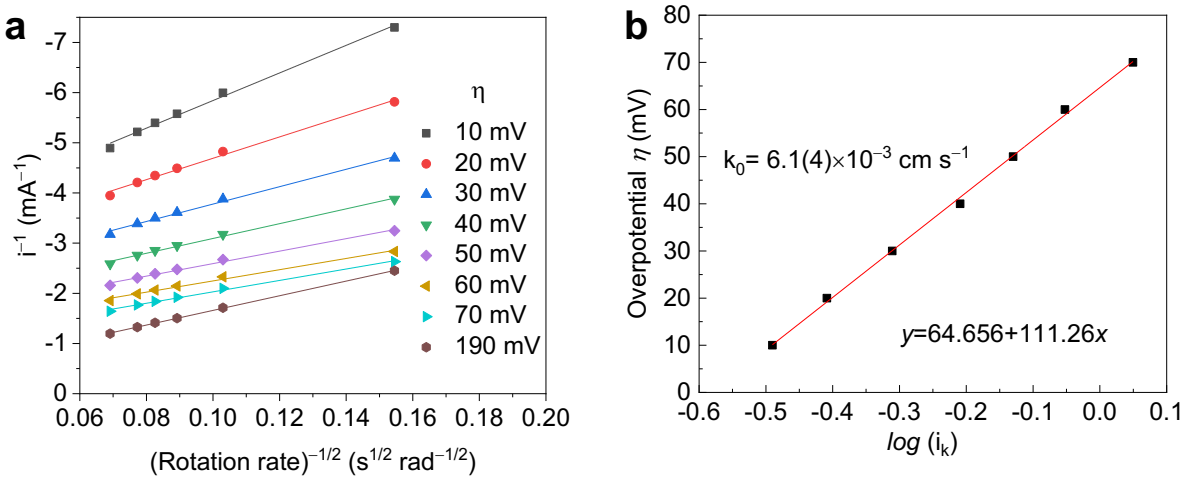

Figure S8. Koutecký–Levich analysis gives the values of mass-transport-independent currents, which result in a standard rate constant k^0 of AQ-1,8-3E-OH 6.1(4) × 10^{-3} cm s^{-1}.

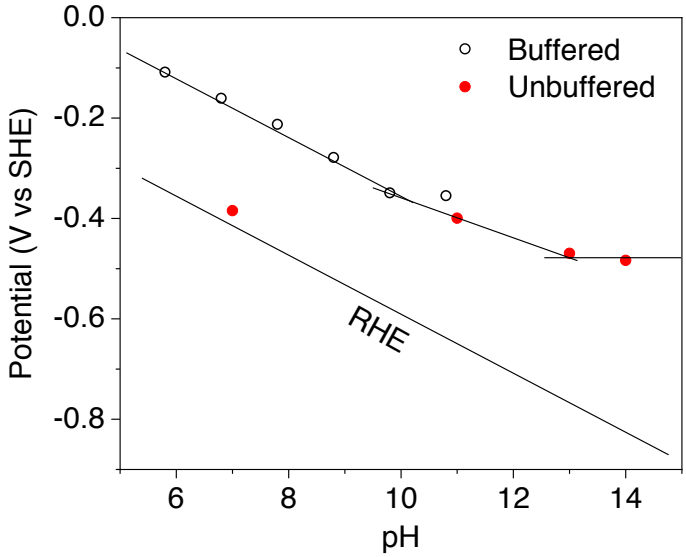

Figure S9. Pourbaix diagram of AQ-1,8-3E-OCH_3 with a slope of –59 mV/pH fit to the data from pH 6-10 and a slope of –29 mV/pH from pH 10-12.5. Above pH ~ 12.5, the potential is pH-independent, indicating that the reduced form of AQ-1,8-3E-OCH_3 is fully deprotonated. All of the potentials were determined by cyclic voltammograms of 10 mM AQ-1,8-3E-OCH_3 in buffered solutions.

Full Cell Measurements

Flow battery experiments were constructed with cell hardware from Fuel Cell Tech. (Albuquerque, NM), assembled into a zero-gap flow cell configuration, similar to a previous report[9]. Pyrosealed POCO graphite flow plates with serpentine flow patterns were used for both electrodes. Each

electrode comprised a 5 cm^2 geometric surface area covered by a stack of four sheets of Sigracet SGL 39AA porous carbon paper pre-baked in air for 24 h at 400 °C.

Full cell cycling was performed with a Fumasep E-620(K) membrane due to its low permeability of AQ-1,8-3E-OH and ferro/ferricyanide. To obtain the polarization curves, the cell was first charged to the desired state of charge and then polarized via linear sweep voltammetry at a rate of 100 mV/s. This method was found to yield polarization curves very close to point-by-point galvanostatic holds, yet to impose minimal perturbation to the SOC of the small-electrolyte-volume cell. Electrochemical impedance spectroscopy (EIS) was performed at SOCs between 10 and 100% at open-circuit potential with a 10 mV perturbation and with frequency ranging from 1 to 300,000 Hz. Three cells with varying negolyte and posolyte concentrations were studied.

1. The negolyte of the 0.1 M cell was prepared by dissolving 0.4 g AQ-1,8-3E-OH (0.79 mmol) into 7.4 mL 1 M KCl solution. The volume of the solution expanded to achieve a 0.1 M AQ solution. The posolyte of the 0.1 M cell was prepared by dissolving 1.69 g $K_4[Fe(CN)_6]\cdot 3H_2O$ (4 mmol) and 0.53 g $K_3[Fe(CN)_6]\cdot 6H_2O$ (1.6 mmol) into 40 mL 1 M KCl to make a 0.1 M ferrocyanide 0.04 M ferricyanide solution.

2. The negolyte of the 1.5 M cell was prepared by dissolving 5.30 g AQ-1,8-3E-OH (0.0105 mol) into 2.4 mL 3 M KCl solution. The volume of the solution expanded to 7 mL to achieve a 1.5 M AQ solution. The posolyte of the 1.5 M cell was prepared by dissolving 19.64 g $K_4[Fe(CN)_6]\cdot 3H_2O$ (0.0465 mol) and 15.31 g $K_3[Fe(CN)_6]\cdot 6H_2O$ (0.0465 mol) into 150 mL 1 M KCl to make a 0.31 M ferrocyanide 0.31 M ferricyanide solution.

3. A negolyte comprising 6 mL 1.5 M AQ-1,8-3E-OH in 0.5 M KCl was paired with 12 mL of a 1.51 M ferrocyanide posolyte comprising 3.81 g $K_4[Fe(CN)_6]\cdot 3H_2O$ (9.03 mmol), 4.37 g $Na_4[Fe(CN)_6]\cdot 10H_2O$ (9.03 mmol) and 0.04 g $K_3[Fe(CN)_6]\cdot 6H_2O$ (0.12 mmol). No additional KCl was added to this solution.

Using the aforementioned cell compositions, we cycled the battery using a sequential potential step method. During charging, voltage limits were set at 1.0, 1.1, and 1.3 V with 160, 100, and 16 mA/cm^2 cutoff current densities, respectively. During discharging, voltage limits were set at 0.8, 0.6, and 0 V with 100, 40, and 4 mA/cm^2 cutoff current densities, respectively. This method was applied to counter the resistance influence of the membranes, electrolytes, electrodes, *etc.* on capacity utilization; because the major purpose is to evaluate the stability of negolyte, the prerequisite is achieving almost full capacity, which was unachievable using the conventional galvanostatic cycling method in this case (**Figure S10**). If >90% of capacity cannot be accessed, the measured capacity fade rate may be underestimated.

Polarization experiments (1.06 V at 50% SOC, Figure 5a and 5b) on the 1.5 M-negolyte cell showed a higher OCV across all SOCs (0.98 V at 50% SOC, Figure 4a and 4b) than with the previous 0.1 M-negolyte cell. This observation may be explained by the following considerations: 1. the higher concentration of negolyte drives the pH of the negolyte to a higher value even at a low SOC, which lowers the reduction potential of AQ-1,8-3E-OH, as a result, increasing the overall voltage of the cell; 2. the ferricyanide/ferrocyanide ratio is 1:1 in the high concentration cell as opposed to 0.4:1 in the low concentration cell, thus giving relatively higher voltage in the

1.5 M-negolyte cell at 0% SOC; 3. The capacity ratio of posolyte to negolyte is different, so that when the negolyte is at 50% SOC, the posolyte is at a higher SOC in the 1.5 M-negolyte cell than in the 0.1 M-negolyte cell.

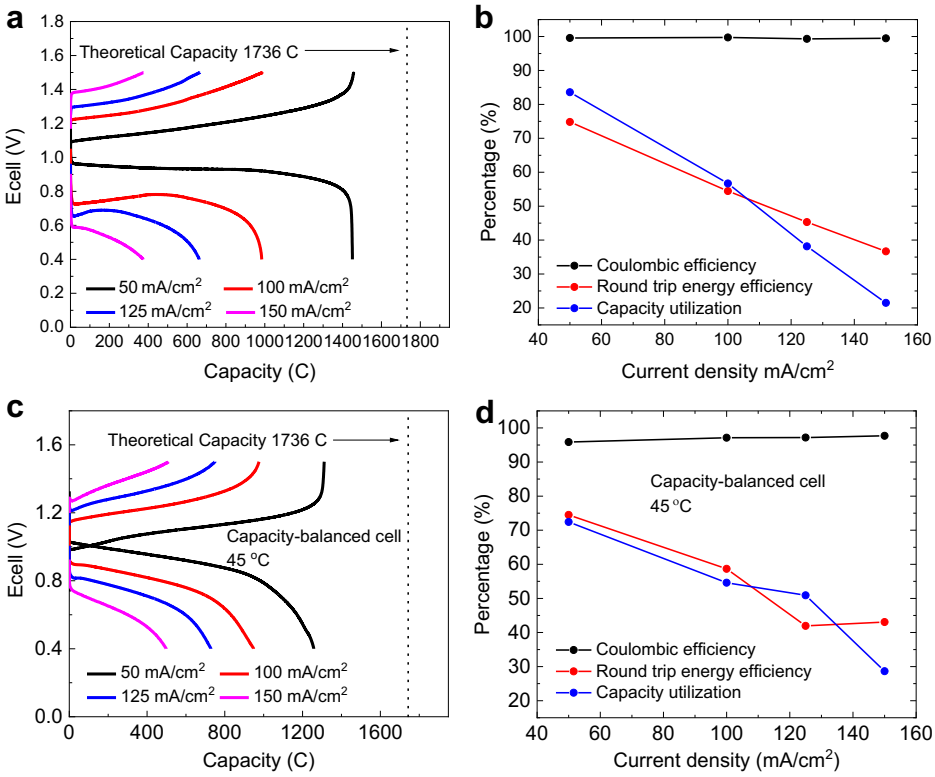

Figure S10. (a) Galvanostatic cycling of 6 mL of a 1.5 M negolyte in 1 M KCl and 40 mL of 1 M ferro/ferricyanide solution (0.5 M $K_4Fe(CN)_6$ + 0.5 M $Na_4Fe(CN)_6$) under 50–150 mA/cm^2 current densities at room temperature. (b) Coulombic efficiency, round trip energy efficiency, and capacity utilization of the 1.5 M negolyte cycling under current densities in (a). (c) Galvanostatic cycling of 6 mL of a 1.5 M negolyte in 0.5 M KCl and 12 mL of 1.51 M ferro/ferricyanide solution (0.755 M $K_4Fe(CN)_6$ + 0.755 M $Na_4Fe(CN)_6$) under 50–150 mA/cm^2 current densities at 45 °C. (d) Current efficiency, energy efficiency, and capacity utilization of the 1.5 M negolyte cycling under current densities in (c).

Decomposition Analysis of AQ-1,8-3E-OH

Although AQ-1,8-3E-OH demonstrates the highest reported capacity, the temporal fade rate is ~50 times higher than that of state-of-the-art molecules[4, 5]. It has been demonstrated that structural stability can be significantly improved with proper molecular modification[4, 24]. Apparently, judicious molecular design relies on a deep understanding of molecular decomposition mechanisms. We analyzed the cycled negolyte for decomposed species. Nuclear magnetic resonance (NMR) spectra of a pristine sample and cycled sample were compared (**Figure S12–13**). A D_2O sample was prepared by diluting 100 µL of a cycled 0.1 M negolyte (**Figure S11**) solution after 18% capacity loss with 700 µL D_2O solvent. A set of three new peaks with chemical shifts δ 7.14 (t), 6.91 (d) and 6.83 (d) ppm with a 1:1:1 integration ratio was observed in the aromatic region, indicating that the new species possesses similar geometry to AQ-1,8-3E-OH (**Figure S13**).

Dividing the integration of the new peaks by the total integration of the aromatic peaks (the sum of AQ-1,8-3E-OH peaks and new peaks), the new peaks correspond to 19% decomposition of AQ-1,8-3E-OH, which coincides with the amount of capacity loss observed after cycling (**Figure S11**). To determine whether any peaks were concealed by the broad water peak centered at 4.79 ppm, we also performed ^{1}H NMR in $CDCl_3$ by extracting the D_2O NMR sample with the same volume of $CDCl_3$. The ratio of the integrals of the peaks corresponding to the decomposition product to those corresponding to AQ-1,8-3E-OH did not change after extraction, indicating that both AQ-1,8-3E-OH and the decomposition product have similar solubility in either solvent (**Figure S14**). A singlet peak with chemical shift δ 5.49 ppm in $CDCl_3$ appeared with an integration value equal to half the integral of each new peak in the aromatic region (*i.e.*, new peaks not present in the NMR spectrum of pristine AQ-1,8-3E-OH). Using this $CDCl_3$ sample, we further performed diffusion ordered spectroscopy (DOSY) and found two well-separated species in the diffusion dimension, except for $CHCl_3$ and H_2O, suggesting that the singlet peak with chemical shift δ 5.49 ppm originated from the same compound that has the three aromatic peaks with chemical shifts δ 7.46 (d), 7.26 (t), and 6.80 (d) ppm (**Figure S16**). DOSY also revealed that the new compound has a smaller diffusion coefficient and hence a larger hydrodynamic radius compared to AQ-1,8-3E-OH. High-resolution LC-MS corroborated the DOSY result by indicating that the only two species in the post-cycling sample are AQ-1,8-3E-OH with m/z 549.1979 (anion of AQ-1,8-3E-OH + formic acid adduct) and a dimer structure with m/z 1023.4233 (anion of a dimer + formic acid adduct).(**Figure S17**) The mass of the decomposition product is twice the mass that would result from subtracting one oxygen from and adding one hydrogen to the mass of AQ-1,8-3E-OH, which suggests that the dimer is a tetra-triethylene glycol-substituted dianthrone. Previous work has identified the crystal structures of two types of dianthrone formed from 1,8-dimethoxy substituted anthraquinones in a reductive environment: 1,1',8,8'-tetramethoxy dianthrone, where the methoxy substituents on the two anthrones are pointing toward each other[25] and 4,4',5,5'-tetramethoxy dianthrone, where the methoxy substituents on the two anthrones are pointing away from each other[24]. The NMR peak chemical shifts in $CDCl_3$ solvent of the aromatic region of the 4,4',5,5'-dimer are identified as ranging from δ 8.0 to 7.16 ppm, and the methine protons have chemical shift δ 6.2 ppm. The chemical shifts of neither of these two regions match what we observed. The aromatic peaks in our case have chemical shifts δ 7.46, 7.26, and 6.80 ppm and the methine peak has chemical shift δ 5.49 ppm. On the other hand, the reported NMR peak chemical shifts for the 1,1',8,8'-tetramethoxy dianthrone have chemical shifts δ 7.42, 7.31, and 6.88 ppm for the aromatic protons and δ 5.85 ppm for the methine protons, both of which comport well with the observed peaks[23]. Hence, we infer that the decomposition product is likely 1,1',8,8'-tetrakis(2-(2-(2-hydroxyethoxy)ethoxy)ethoxy)-[9,9'-bianthracene]-10,10'(9*H*,9'*H*)-dione.

We then sought to determine whether the oxidized or the reduced form of AQ-1,8-3E-OH contributed more to the decomposition. Two solutions of 0.1 M AQ-1,8-3E-OH in 1 M KCl, one uncharged and the other charged, were stored in a glovebox at room temperature for two weeks. The charged sample was discharged in air after the two-week period, and both samples were extracted with $CDCl_3$. The ^{1}H NMR spectrum of the uncharged sample showed no evidence of decomposition, whereas the spectrum of the charged sample included peaks corresponding to the dimer in the aromatic region with integration 18% that of the AQ-1,8-3E-OH aromatic peaks, representing a decomposition rate of 1.1%/day (**Figure S15**). This temporal fade rate is ~2 times the rate of 0.5%/day observed in long-term flow cell cycling, which is reasonable, as reduced AQ-1,8-3E-OH accounts for 50% of the total time during cycling. Therefore, we conclude that the

decomposition of the charged form of AQ-1,8-3E-OH is responsible for the observed capacity fade in flow cells.

Four decomposition pathways were proposed as described in **Scheme S1**. Structural optimization and energy calculations of the optimized structures were performed using Gaussian 16, M06/3-21G method/basis-set with Solvation Model based on Density (SMD). The computational results suggest that the dimerization is a thermodynamically favorable process. The intermediate species of routes I and III have lower energy, suggesting more favorable kinetics of these two routes (assuming that the relatively lower energies of the intermediates reflect relatively lower energy transition states as well).

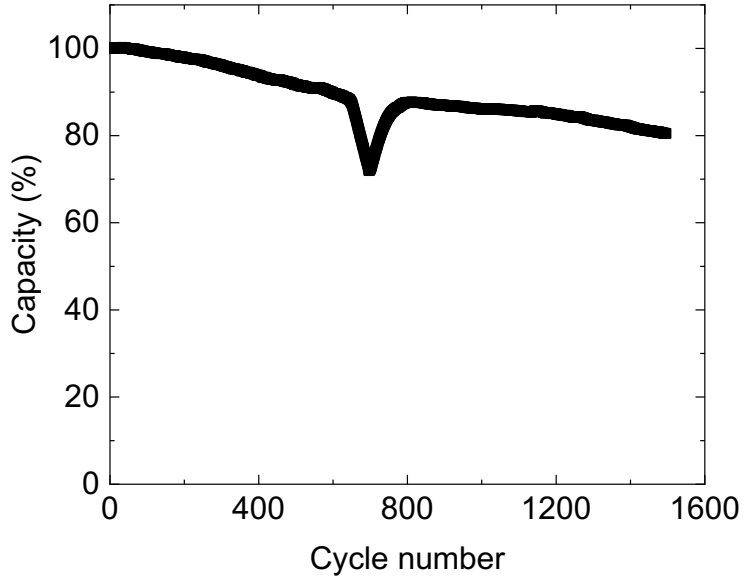

Figure S11. The discharge capacity of a full cell comprising 0.1 M AQ-1,8-3E-OH in 1 M KCl *vs.* 0.1 M ferrocyanide for 1500 cycles shows 18% capacity fade. The capacity drop from cycle number 600–800 was caused by depletion of nitrogen gas.

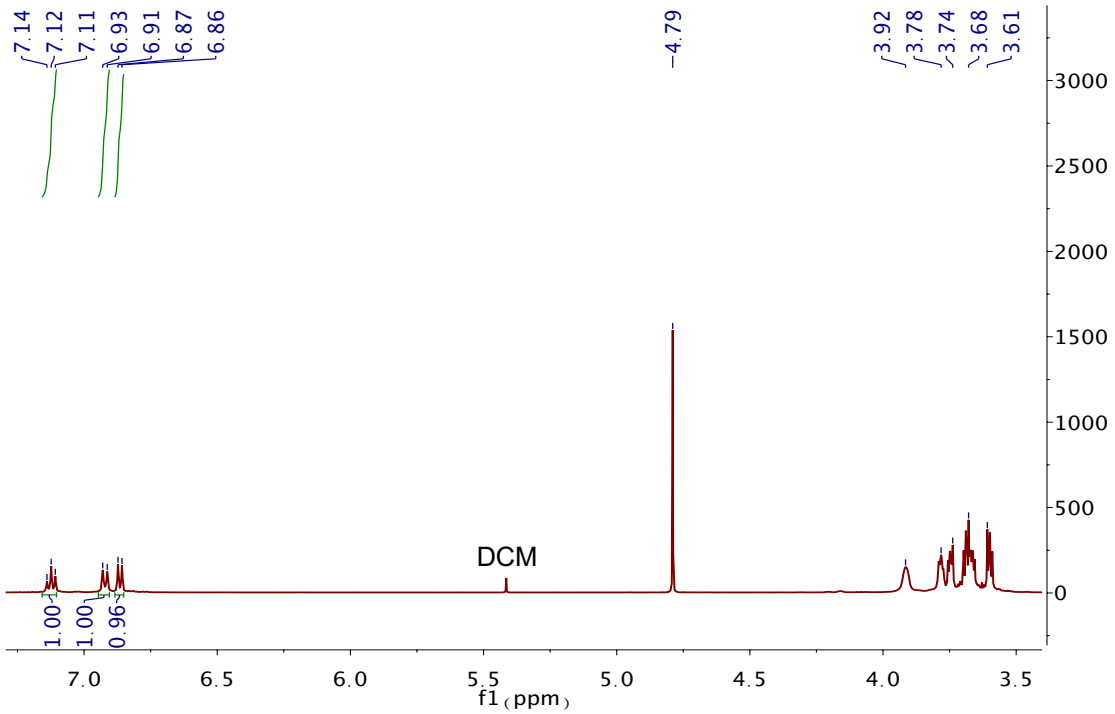

Figure S12. ^{1}H NMR of pristine AQ-1,8-3E-OH in D_2O. The integration of the aromatic protons of AQ-1,8-3E-OH is shown.

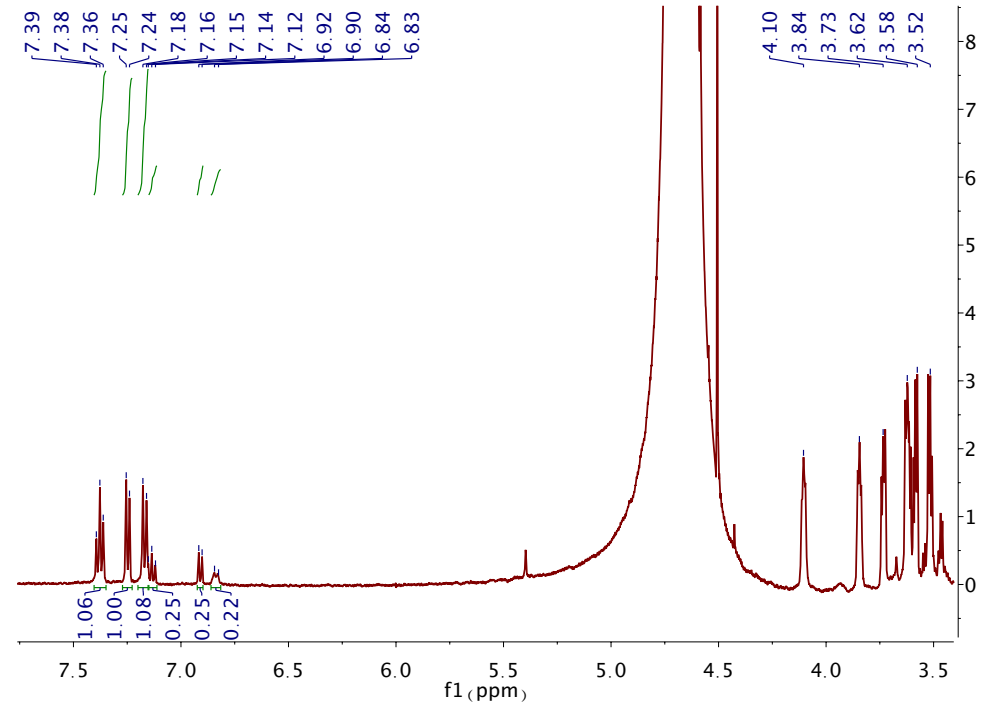

Figure S13. ^{1}H NMR of cycled AQ-1,8-3E-OH in D_2O. The integration of the aromatic protons of AQ-1,8-3E-OH and the decomposition product are shown, indicating 19% decomposition. The large peak corresponding to H_2O conceals some peaks corresponding to the decomposition product.

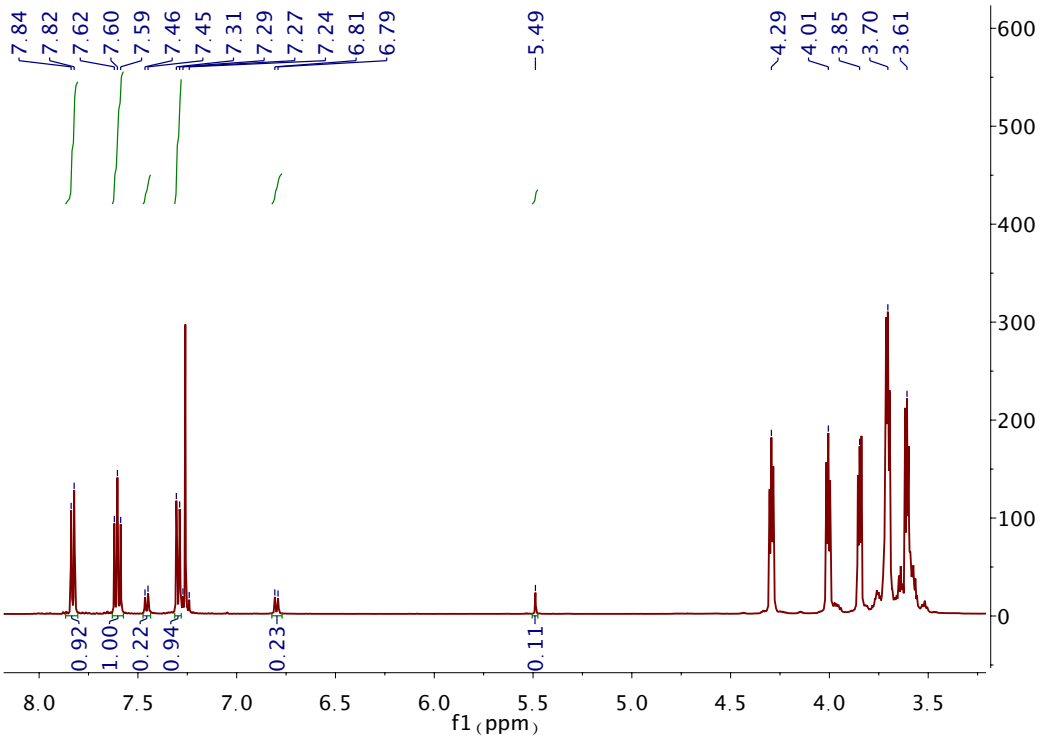

Figure S14. The ^{1}H NMR spectrum of cycled AQ-1,8-3E-OH in $CDCl_3$. The integration and corresponding ratio are the same as the one in D_2O, suggesting that all the pristine and decomposition compounds are extracted successfully. The integration of the peak at a chemical shift of 5.49 ppm (methine proton peak) is half of the integration of one of the aromatic peaks in the decomposition compound.

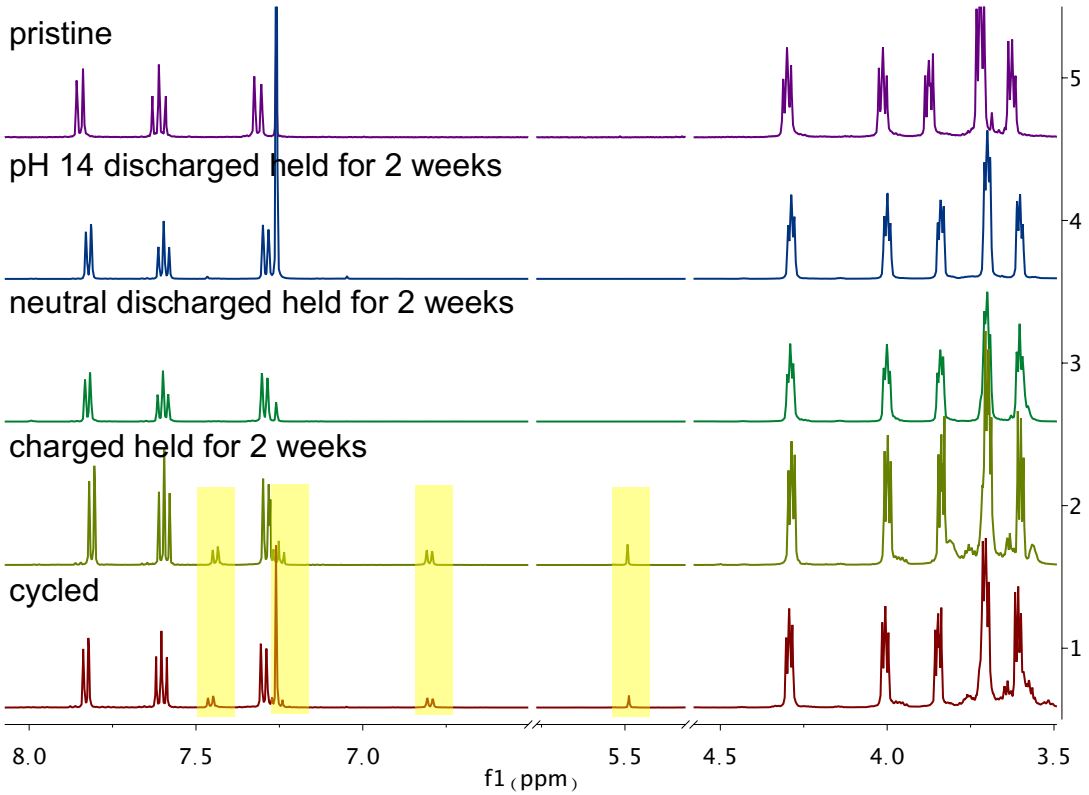

Figure S15. Comparison of ^{1}H NMR spectra (in $CDCl_3$) of pristine, discharged-held, charged-held, and cycled AQ-1,8-3E-OH. The spectrum of the charged-held sample is identical to the spectrum of the cycled sample, while the spectra from both pristine and the discharged-held samples are exactly the same, indicating the decomposition of the charged AQ-1,8-3E-OH is the major reason for capacity fading.

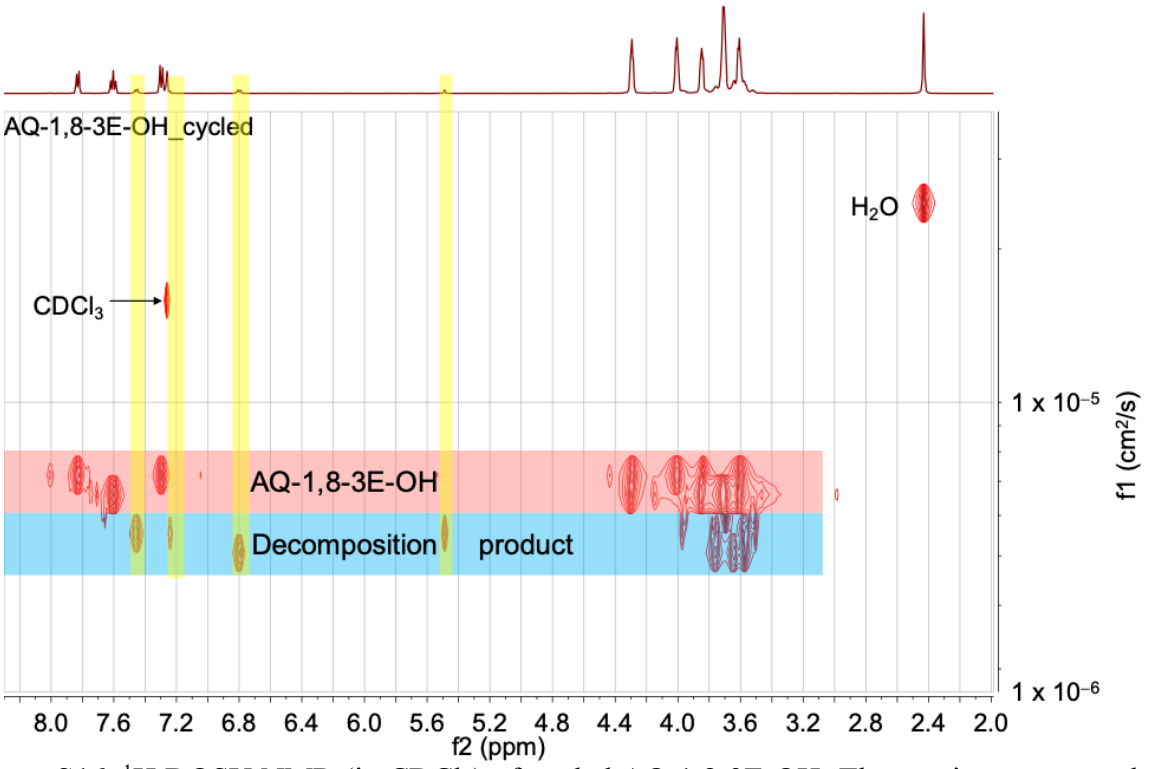

Figure S16. ^{1}H DOSY NMR (in $CDCl_3$) of cycled AQ-1,8-3E-OH. The *x*-axis represents the ^{1}H chemical shift, and the *y*-axis represents the relative diffusion rate. The spectrum shows two species with different diffusion coefficients. The decomposition product has a smaller diffusion coefficient compared to AQ-1,8-3E-OH, which suggests that the decomposition product has a larger hydrodynamic radius.

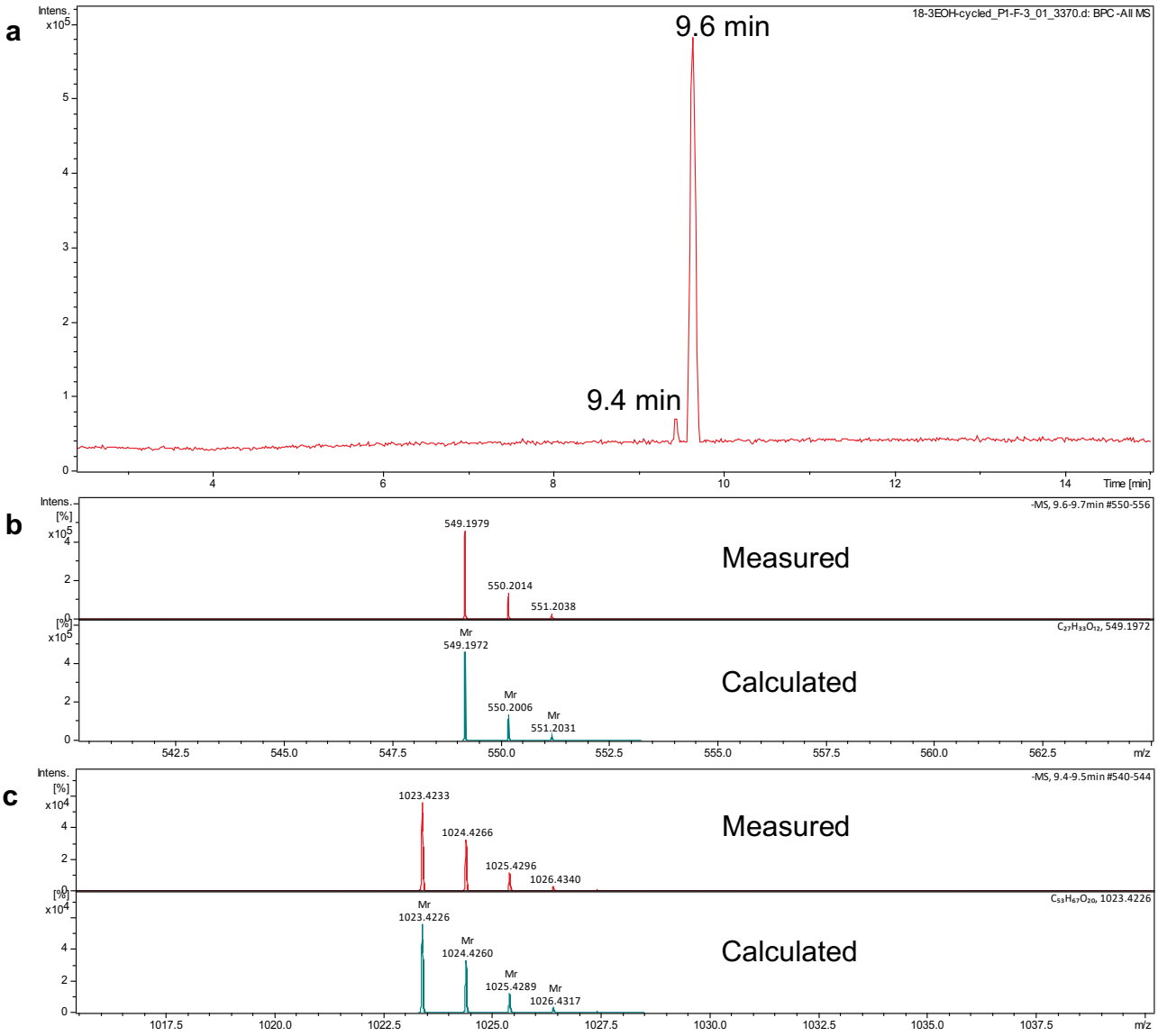

Figure S17. (a) High resolution LC–MS (negative mode) spectrum of the cycled sample shows the presence of two species eluted from the LC column with retention times of 9.6 and 9.4 minutes, respectively. (b) The former has a mass/charge ratio of 549.1979, corresponding to the mass of AQ-1,8-3E-OH plus a formic acid adduct, and (c) the latter has a mass/charge ratio of 1023.4233, corresponding to the mass of 1,1',8,8'-tetrakis(2-(2-(2-hydroxyethoxy)ethoxy)ethoxy)-[9,9'-bianthracene]-10,10'(9*H*,9'*H*)-dione plus a formic acid adduct. The existence of isotopes generates a cluster of peaks (isotope peaks); all peaks in a cluster are of the same molecular formula.

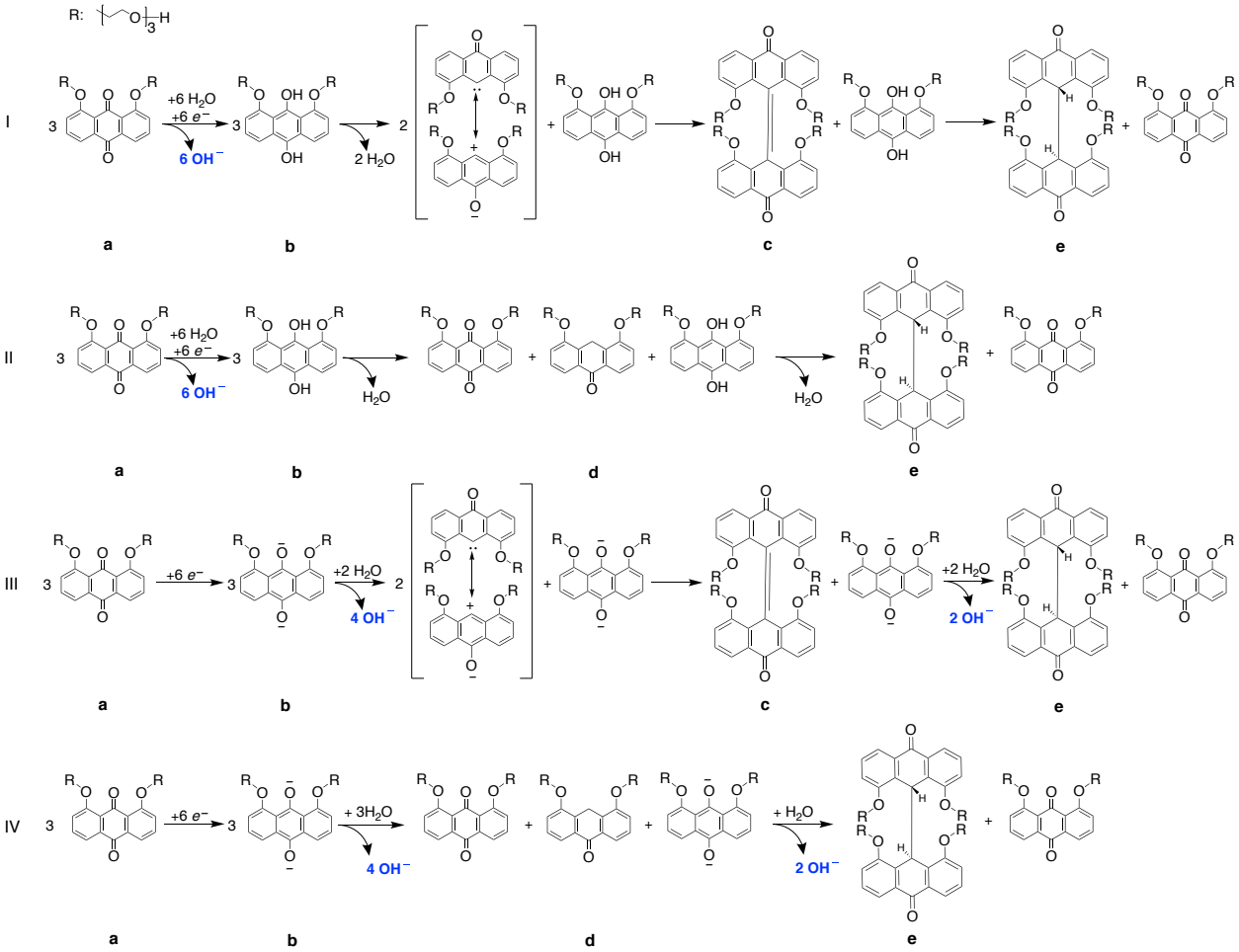

Scheme S1. Proposed decomposition pathways. In pathways I and II, the reduced AQ is protonated, and in pathways III and IV, it is not. In pathways I and III, the reduced AQ is directly dimerized. In pathways II and IV, PEG-anthrone forms first and then dimerizes in a second step.

Table S3. Calculated energy, using Gaussian 16, M06/3-21G method/basis-set with SMD, for each species in the decomposition pathway as shown in **Scheme S1**. *Energy refers to electronic energy.

Name	Energy* (Hartree)
a. 1,8-bis(2-(2-(2-hydroxyethoxy)ethoxy)ethoxy)anthracene-9,10-dione	-1751.915
b. 1,8-bis(2-(2-(2-hydroxyethoxy)ethoxy)ethoxy)anthracene-9,10-diol	-1753.115
c. 1,1',8,8'-tetrakis(2-(2-(2-hydroxyethoxy)ethoxy)ethoxy)-10H,10'H-[9,9'-bianthracenylidene]-10,10'-dione	-3354.245
d. 4,5-bis(2-(2-(2-hydroxyethoxy)ethoxy)ethoxy)anthracen-9(10H)-one	-1678.298
e.1,1',8,8'-tetrakis(2-(2-(2-hydroxyethoxy)ethoxy)ethoxy)-[9,9'-bianthracene]-10,10'(9H,9'H)-dione	-3355.499
H_2O	-75.968

Table S4. Calculated energy, using Gaussian 16, M06/3-21G method/basis-set with SMD, for the initial, intermediate, and final states. The differences in electronic energy, ΔE, compared with the initial state are listed in column 3.

State	Energy (Hartree)	ΔE (kcal/mol)
Initial: 3***b**	-5259.346	0
Path A intermediate: **c**+**b**+2*H_2O	-5259.298	30.642
Path B intermediate: **a**+**b**+**d**+H_2O	-5259.297	31.101
Final: **a**+**e**+2*H_2O	-5259.351	-2.573

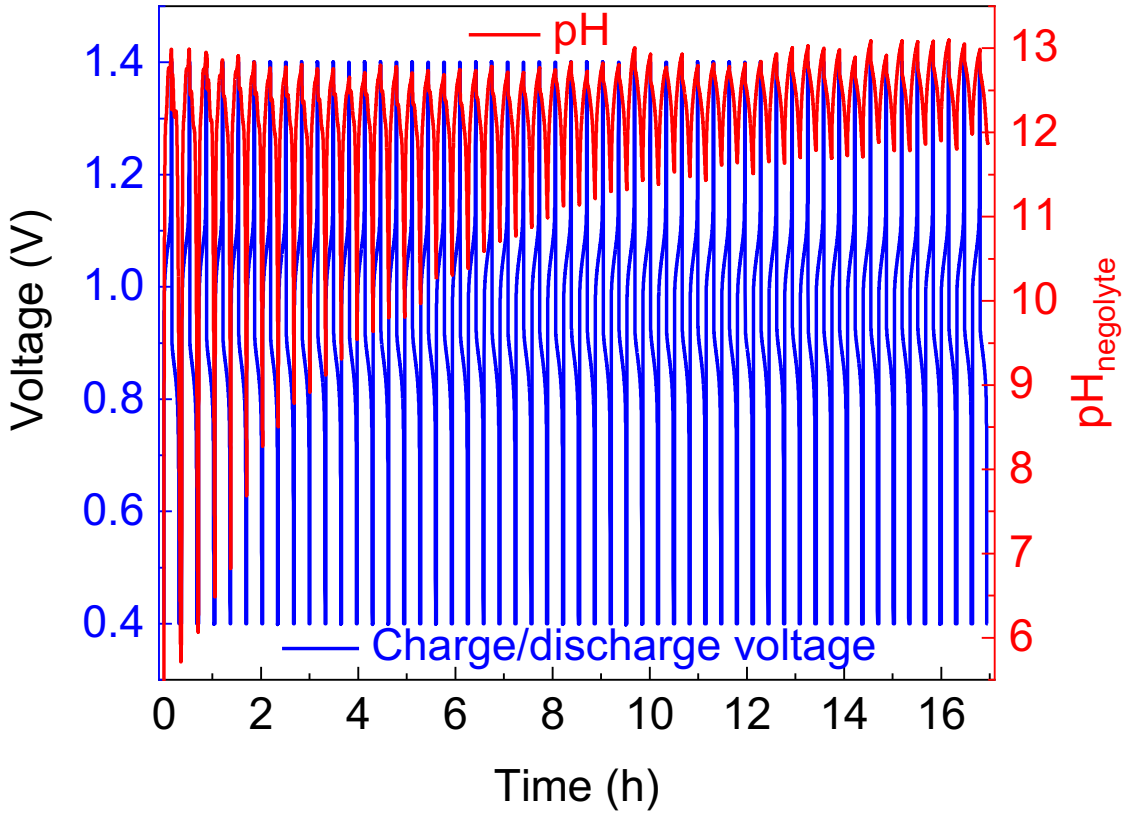

Figure S18. Irreversible pH change during long term cycling in a glovebox is explained by the hydroxide generation associated with the decomposition of charged AQ-1,8-3E-OH. Electrolytes comprised 7 mL of 0.1 M AQ-1,8-3E-OH (negolyte) in 1 M KCl and 40 mL of 0.1 M potassium ferrocyanide and 0.04 M ferricyanide (posolyte) in 1 M KCl. The applied current density was 50 mA/cm^2.

Cost Considerations

The mass production cost of AQ-1,8-3E-OH is presently unknown, but the expected price is similar to that of 1,8-DHAQ since the synthesis is a facile one-step Williamson etherification with cheap halogenated-ethylene-oxide as a reagent. In addition, at industrial scale, purification through column chromatography is likely unnecessary when reaction temperature and time are optimized to produce purer products in a one-pot reaction. Therefore, the cost of 1,8-DHAQ should be the dominant component in the production of AQ-1,8-3E-OH. Danthron, or 1,8-DHAQ, is found in green vegetables and widely used as precursor for dye molecules. Although the market price for mass-produced 1,8-DHAQ is unknown, current prices for lab-scale 1,8-DHAQ from Sigma Aldrich, AK Scientific, and TCI America are \$0.274/g, \$0.226/g, and \$0.814/g, respectively, which are, on average, more than fifty times cheaper than corresponding values for 2,6-DHAQ. Therefore, we expect the mass-production price for 1,8-DHAQ also to be lower than that for 2,6-DHAQ, which was projected to be \$0.92/kg–\$3.92/kg[10, 5]. Yuan *et al.*[25] reported the cost of sodium ferrocyanide as \$1.07/kg; therefore, the large-scale cost of material is expected to be quite

low. Costs should be further reduced by the use of a non-fluorinated membrane and by the absence of strong base or acid in the electrolyte, enabling the use of less corrosion-resistant electrolyte-contacting materials.

Supplementary References

1. Suttil, J. A.; Kucharyson, J. F.; Escalante-Garcia, I. L.; Cabrera, P. J.; James, B. R.; Savinell, R. F.; Sanford, M. S.; Thompson, L. T. Metal Acetylacetonate Complexes for High Energy Density Non-aqueous Redox Flow Batteries. *Journal of Materials Chemistry A* **2015,** *3* (15), 7929–7938.
2. Kwon, G.; Lee, S.; Hwang, J.; Shim, H.-S.; Lee, B.; Lee, M. H.; Ko, Y.; Jung, S.-K.; Ku, K.; Hong, J.; Kang, K. Multi-redox Molecule for High-Energy Redox Flow Batteries. *Joule* **2018**, 2, 1771–1782.
3. Hu, B.; Liu, T. L. Two Electron Utilization of Methyl Viologen Anolyte in Nonaqueous Organic Redox Flow Battery. *Journal of Energy Chemistry* **2018,** *27* (5), 1326–1332.
4. Ji, Y.; Goulet, M-A.; Pollack, D. A.; Kwabi, D. G.; Jin, S.; De Porcellinis, D.; Kerr, E. F.; Gordon, R. G.; Aziz, M. J. A Phosphonate-Functionalized Quinone Redox Flow Battery at Near-Neutral pH with Record Capacity Retention Rate. *Adv. Energy Mater.* **2019**, *9*, 1900039.
5. Kwabi, D. G.; Lin, K.; Ji, Y.; Kerr, E. F.; Goulet, M.-A.; Porcellinis, D. D.; Tabor, D. P.; Pollack, D. A.; Aspuru-Guzik, A.; Gordon, R. G.; Aziz, M. J. Alkaline Quinone Flow Battery with Long Lifetime at pH 12. *Joule* **2018,** *2* (9), 13.
6. Yang, B.; Hoober-Burkhardt, L.; Wang, F.; Surya Prakash, G. K.; Narayanan, S. R. An Inexpensive Aqueous Flow Battery for Large-scale Electrical Energy Storage Based on Water-soluble Organic Redox Couples. *Journal of the Electrochemical Society* **2014,** *161*, A1371–A1380.
7. Wei, X.; Duan, W.; Huang, J.; Zhang, L.; Li, B.; Reed, D.; Xu, W.; Sprenkle, V.; Wang, W. A High-current, Stable Nonaqueous Organic Redox Flow Battery. *ACS Energy Letters* **2016,** *1* (4), 705–711.
8. Hollas, A.; Wei, X.; Murugesan, V.; Nie, Z.; Li, B.; Reed, D.; Liu, J.; Sprenkle, V.; Wang, W. A Biomimetic High-Capacity Phenazine-Based Anolyte for Aqueous Organic Redox Flow Batteries. *Nature Energy* **2018,** *3* (6), 508–514.
9. Lin, K.; Chen, Q.; Gerhardt, M. R.; Tong, L.; Kim, S. B.; Eisenach, L.; Valle, A. W.; Hardee, D.; Gordon, R. G.; Aziz, M. J.; Marshak, M. P. Alkaline Quinone Flow Battery. *Science* **2015,** *349* (6255), 5.
10. Yang, Z.; Tong, L.; Tabor, D. P.; Beh, E. S.; Goulet, M.-A.; Porcellinis, D. D.; Aspuru-Guzik, A.; Gordon, R. G.; Aziz, M. J. Alkaline Benzoquinone Aqueous Flow Battery for Large-Scale Storage of Electrical Energy. *Adv. Energy Mater.* **2018**, *8*, 1702056.
11. Lin, K.; Gómez-Bombarelli, R.; Beh, E. S.; Tong, L.; Chen, Q.; Valle, A.; Aspuru-Guzik, A.; Aziz, M. J.; Gordon, R. G. A Redox-flow Battery with an Alloxazine-based Organic Electrolyte. *Nature Energy* **2016,** *1* (9), 16102.
12. Hu, B.; DeBruler, C.; Rhodes, Z.; Liu, T. Leo Long-cycling Aqueous Organic Redox Flow Battery (AORFB) Toward Sustainable and Safe Energy Storage. *Journal of the American Chemical Society* **2017,** *139* (3), 1207–1214.
13. Wei, X.; Duan, W.; Huang, J.; Zhang, L.; Li, B.; Reed, D.; Xu, W.; Sprenkle, V.; Wang, W. A High-current, Stable Nonaqueous Organic Redox Flow Battery. *ACS Energy Letters* **2016,** *1* (4), 705–711.

14. Luo, J.; Hu, B.; Debruler, C.; Bi, Y.; Zhao, Y.; Bing, Y.; Hu, M.; Wu, W.; Liu, T. L. Unprecedented Capacity and Stability of Ammonium Ferrocyanide Catholyte in pH Neutral Aqueous Redox Flow Batteries. *Joule* **2019,** *3*, 149–163.
15. Beh, E. S.; De Porcellinis, D.; Gracia, R. L.; Xia, K. T.; Gordon, R. G.; Aziz, M. J. A Neutral pH Aqueous Organic–Organometallic Redox Flow Battery with Extremely High Capacity Retention. *ACS Energy Lett.* **2017,** *2* (3), 639–644.
16. Huskinson, B.; Marshak, M. P.; Suh, C.; Er, S.; Gerhardt, M. R.; Galvin, C. J.; Chen, X.; Aspuru-Guzik, A.; Gordon, R. G.; Aziz, M. J. A Metal-free Organic-Inorganic Aqueous Flow Battery. *Nature* **2014,** *505* (7482), 195–8.
17. Ponce de León, C.; Frías-Ferrer, A.; González-García, J.; Szánto, D. A.; Walsh, F. C. Redox Flow Cells for Energy Conversion. *Journal of Power Sources* **2006,** *160* (1), 716–732.
18. Janoschka, T.; Martin, N.; Hager, M. D.; Schubert, U. S. An Aqueous Redox-Flow Battery with High Capacity and Power: The TEMPTMA/MV System. *Angew. Chem. Int. Ed.* **2016,** *55* (46), 14427–14430.
19. Li, L.; Kim, S.; Wang, W.; Vijayakumar, M.; Nie, Z.; Chen, B.; Zhang, J.; Xia, G.; Hu, J.; Graff, G.; Liu, J.; Yang, Z. A Stable Vanadium Redox-Flow Battery with High Energy Density for Large-Scale Energy Storage. *Adv. Energy Mater.* **2011,** *1*, 7.
20. Hall, J.; Perkin, A. G., Reduction Products of the Hydroxyanthraquinones Part II. *Journal of the Chemical Society, Transactions* **1923**, *123*, 2029–2037.
21. Giguere, J. B.; Morin, J. F. New Strapped Porphyrins as Hosts for Fullerenes: Synthesis and Complexation Study. *Org. Biomol. Chem.* **2012,** *10* (5), 1047–51.
22. Kestin, J.; Khalifa, H. E.; Correia, R. J. Tables of the Dynamic and Kinematic Viscosity of Aqueous KCl Solutions in the Temperature Range 25-150 ºC and the Pressure Range 0.1-35 MPa. *J. Phys. Chem. Ref. Data* **1981,** *10*, 15.
23. Shi, Z.; Li, Y.; Li, Y.; Lu, G.; Liu S. 1,1',8,8'-Tetramethoxy-10,10'-Bianthrone. *Acta Cryst.* **2004,** *E60*, 7.
24. Shyamasundar, N.; Caluwe, P.; Lithium Aluminum Hydride Reduction of peri-alkoxy-9,10-anthraquinones. *Journal of Organic Chemistry* **1981,** *46*, 6.
25. Yuan, Z.; Duan, Y.; Liu, T.; Zhang, H.; Li, X. Toward a Low-Cost Alkaline Zinc-Iron Flow Battery with a Polybenzimidazole Custom Membrane for Stationary Energy Storage. *iScience* **2018,** *3*, 40-49.